ERBIUM DOPED III-N MATERIALS FOR NEAR-IR OPTOELECTRONICS

By

J. DEVIN MACKENZIE

A DISSERTATION PRESENTED TO THE GRADUATE SCHOOL
OF THE UNIVERSITY OF FLORIDA IN PARTIAL FULFILLMENT
OF THE REQUIREMENTS FOR THE DEGREE OF
DOCTOR OF PHILOSOPHY

UNIVERSITY OF FLORIDA

1998

ACKNOWLEDGMENTS

The author owes an incredible debt to Prof. Cammy R. Abernathy. Without her support from the first day of graduate school to the last, this could not have been possible. Even in the most difficult times, the value of the academic and personal relationship with her was undeniable. The author is also indebted to Prof. Kirk Kolenbrander and Prof. Reza Abbaschian for leading him to Cammy's door. In the future, the author could not hope to work with someone more capable, understanding or uncannily reasonable than Prof. Abernathy. Thanks.

Many thanks are also due to the many collaborators who have contributed to this work including: Prof. Stephen Pearton, Dr. Uwe Hommerich and his group, Prof. Fan Ren, Dr. Robert Wilson, Dr. Robert Schwartz, Dr. John Zavada, Dr. Paul Chen, Prof. Len Brillson and his group, Sean Donovan, Craig Schardt and W. Krishnamoorthy.

TABLE OF CONTENTS

ACKNOWLEDGMENTS...i

ABSTRACT v

CHAPTERS

1 INTRODUCTION: NEAR IR TECHNOLOGIES AND THE III-N SEMICONDUCTORS 1

2 GROUP III-N GROWTH BY PLASMA-ASSISTED METALORGANIC MOLECULAR BEAM EPITAXY 12

2.1 A Brief History of III-N Research 12
2.2 Metalorganic Molecular Beam Epitaxy of III-N Semiconductors 13
2.3 The Metalorganic Molecular Beam Epitaxy Growth System 17
2.4 Vaccuum Systems 24
2.5 General Growth Procedures 27
2.6 Characterization 30

3 OPTIMIZATION OF III-N GROWTH BY PLASMA-ASSISTED METALORGANIC MOLECULAR BEAM EPITAXY.. 34

3.1 An Optimization Study of Metalorganic Molecular Beam Epitaxy of Aluminum Nitride and Gallium Nitride Semiconductors 34
3.2 Alternative Oxide Substrates for III-N Heteroepitaxy.. 47
3.3 Plasma Characteristics and the Growth of Group III-Nitrides by Metalorganic Molecular Beam Epitaxy 54

4 ALUMINUM NITRIDE DOPED WITH ERBIUM DURING GROWTH BY PLASMA-ASSISTED METALORGANIC MOLECULAR BEAM EPITAXY 67

5 GROWTH AND LUMINESCENCE PROPERTIES OF GALLIUM NITRIDE DOPED WITH ERBIUM DURING DEPOSITION BY PLASMA-ASSISTED METALORGANIC MOLECULAR BEAM EPITAXY... 78

6 OPTICAL AND ELECTRICAL EXCITATION OF METALORGANIC MOLECULAR BEAM EPITAXY-DERIVED GaN:Er STRUCTURES INTEGRATED WITH SILICON 90

REFERENCES 109

BIOGRAPHICAL SKETCH 115

Abstract of Dissertation Presented to the Graduate School
of the University of Florida in Partial Fulfillment of the
Requirements for the Degree of Doctor of Philosophy

ERBIUM DOPING OF III-N MATERIALS FOR NEAR-IR OPTOELECTRONICS

By

J. Devin MacKenzie

August 1998

Chairman: Professor Cammy R. Abernathy
Major Department: Materials Science and Engineering

In this dissertation, the potential for III-N:Er materials, epitaxially-grown in ultrahigh vacuum, as a basis for near-IR optoelectronic devices integrated with Si has been demonstrated. This research effort's scope includes the development and understanding of III-N matrix growth from chemical beams in ultrahigh vacuum, the demonstration and study of the incorporation and luminescence behavior of Er in III-N materials, and finally, the realization of electroluminescent GaN:Er structures emitting at 1.54 μm. Exploitation of the 1.54 μm intra-4f shell transition of the Er^{3+} ion is of immediate technological significance as this radiative transition matches the attenuation loss minima of silica fibers. A III-N device, utilizing Er as an optical center and compatible with economically-developed Si technology, could provide an efficient, temperature stable, and inexpensive light source for fiber communications systems as well as for high speed optical interconnects at all levels of computer integration. Metalorganic molecular beam epitaxy (MOMBE), the growth technique used in this work, was ideally suited for this research as it allowed for growth from elemental beams, metalorganic precursors, and radio-frequency (RF) and electron cyclotron resonance (ECR) plasmas over a range of operating conditions. Also, the MOMBE apparatus provides the capability to tailor device and materials parameters such as rare-earth and electrical dopant profiles and impurity levels.

High quality, GaN and AlN films were grown epitaxially on (0001) Al_2O_3. Optimized growth conditions were determined for growth of III-N materials from ECR and RF nitrogen plasmas. Control over impurity backgrounds through the use of various Group III sources was achieved. Plasma parameters were correlated with film characteristics and optical emission spectra of the RF and ECR plasmas to deduce the optimal Group V conditions for growth. Solid source doping and metalorganic sources were utilized to introduce Er into III-N films during growth. For the first time, strong, room-temperature 1.54 μm photoluminescence (PL) was observed from AlN, InN, GaN and InAlN doped with Er during growth. Device structures fabricated from MOMBE-derived GaN:Er demonstrated, for the first time, electroluminescence at room temperature from III-N:Er materials integrated with Si. Also, for the first time, electroluminescence has been observed from InAlN:Er-based Schottky structures on Si. Luminescence, growth and implantation experiments were performed to deduce the interaction between optically active Er and carbon and oxygen. An acceptor-like energy-transfer state model associated with C has been proposed to explain the optical activation of Er in MOMBE-derived GaN.

CHAPTER 1
INTRODUCTION: NEAR IR TECHNOLOGIES AND THE III-N SEMICONDUCTORS

The revolutionary impact of microelectronics in the second half of this century can be seen at every level of modern society. From the outset, it was the intuition and vision of telecommunications research that sired the microcomputer. In turn, the development of computer and information networks in the private, commercial, and military sectors have placed intense demands on the essential technologies of high data-rate communication. On a smaller scale, the trend towards smaller feature sizes, higher clock speeds and increasing levels of integration in microprocessors is driving chip level communications to the practical and theoretical limits of metallization-interconnect microtechnology. The answer to both of these technical dilemmas may be the photon. Driven by the economics of bandwidth, fiber-optics systems have revolutionized long distance communications. As the information demand continues to grow on an increasingly-local scale, it seems likely that optical communications systems may become increasingly conspicuous fixtures in businesses, schools and homes. Likewise, optical interconnects have the potential to meet the speed and density requirements of GHz-level clock speeds and monolithic integration of complete computing systems.[3]

Optical communications systems have been designed to operate in the optimal wavelength regimes for minimum signal attenuation and dispersion. The near infrared loss spectrum for silica fibers is shown in Figure 1-1.[1] Radiative intra-4f shell transitions in Er^{3+} at 1.54 μm, allowed by crystal field splitting of degenerate levels match the attenuation loss minima in

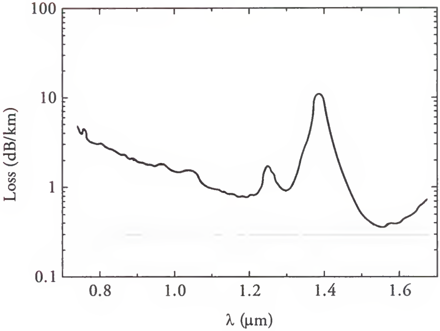

FIGURE 1-1 Silica fiber signal attenuation in the near IR[1]

silica fibers. These energy levels are depicted in Figure 1-2.[2] A similar core-electron transition in the Pr^{3+} ion produces radiative emission at 1.3 μm, the silica dispersion minima, which is another significant optical carrier for fiber communications systems. The energies of these intra-4f shell transitions in the rare-earth ions are quite stable due to the shielding of the 4f shell levels by the filled outer 5s and 5p orbitals. Table 2 lists the electron configurations of the 5s, 5p, and 4f orbitals for the rare-earth ions.[5] As the atomic number increases, the occupation of the valence $5s^2p^6$ shell remains the same while each successive electron in the rare-earth series fills the 4f orbitals. This orbital filling sequence results in very similar chemical properties for all of the rare-earths but a rich optical structure that is unique to each ion. Important for optoelectronics, these intra-4f shell transition energies are effectively shielded from matrix effects by the 5s and 5p

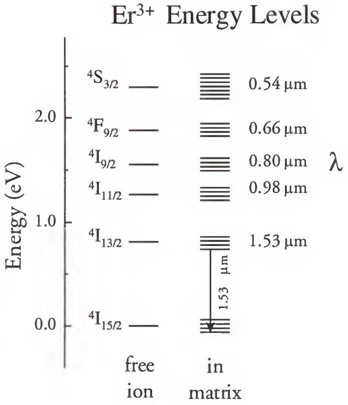

FIGURE 1-2. Configuration of intra-4f shell energy levels in the free Er^{3+} ion and after crystal field splitting of the Er^{3+} levels in a matrix.[2]

electrons. Therefore, the emission wavelength of these rare-earth transitions are largely independent of the host material.

High gain band-edge and multiple quantum-well lasers and detectors based on the InGaAsP/InP materials system were also developed in order to take advantage of the optimum infrared communication wavelength regimes.[6] However, systems based on narrow-gap InGaAsP active materials suffer from poor wavelength stability due to operation-induced temperature drift of the emission line. Also, integration of InGaAsP devices with Si microelectronics for on-chip interconnects is a complex task. The large lattice-mismatch of InGaAsP with Si and the sensitivity of these materials to defects precludes any direct, monolithic integration by epitaxial growth.[7] Other integration strategies based on physically bonding prefabricated, discrete optical components to a Si substrate would be complex, expensive and difficult to implement in applications such as microprocessors or digital signal processing components that would require a high density of interconnects.

Optical fiber systems achieving gain through stimulated emission from optically pumped rare-earth ions were developed to amplify signals in the optical domain.[8] These systems, known as rare-earth doped fiber amplifiers, do not suffer from the temperature stability problems of semiconductor systems based on band-edge emission. The effectiveness of this technology has led to Er-doped fiber amplifiers becoming well established in the long distance telecommunications industry. However, driving forces for simpler, more efficient, less expensive and electronically-integrated 1.54 μm generation and amplification have stimulated interest in developing alternative technologies. The optical pumping systems required in rare-earth-doped fiber amplifier systems can be expensive and large. Also, typical fiber systems have an optical

TABLE 2: OUTER ELECTRON CONFIGURATION OF RARE-EARTH^{3+}IONS

Atomic Number	Element	Electron Configuration
57	Lanthanum	$4f^05s^2p^6$
58	Cerium	$4f^15s^2p^6$
59	Praseodymium	$4f^25s^2p^6$
60	Neodymium	$4f^35s^2p^6$
61	Promethium	$4f^45s^2p^6$
62	Samarium	$4f^55s^2p^6$
63	Europium	$4f^65s^2p^6$
64	Gadolinium	$4f^75s^2p^6$
65	Terbium	$4f^85s^2p^6$
66	Dysprosium	$4f^95s^2p^6$
67	Holmium	$4f^{10}5s^2p^6$
68	Erbium	$4f^{11}5s^2p^6$
69	Thulium	$4f^{12}5s^2p^6$
70	Ytterbium	$4f^{13}5s^2p^6$
71	Lutecium	$4f^{14}5s^2p^6$

interaction length on the order of meters in order to produce the desired amplification.[1] Efforts have been made to reduce the size of these Er-doped optical domain systems and integrate them with Si microelectronics processing technology through the use of planar waveguide technologies. An example of such a device is depicted in Figure 1-3. Although impressive demonstrations of planar waveguide technologies have shown signal coupling, multiplexing and amplification, these devices still require considerable interaction lengths to produce strong optical effects.[4] The surface area that planar waveguide-based devices require may be prohibitive where high interconnect densities are required. Also, many of these devices require high power external laser pump sources.

Considerable research has focused on the development of optoelectronic components based on Er doping of Si[1,2] and III-V materials[3-5] to meet the requirements for simple, economical, and efficient fiber pump sources and integrated local interconnects. Ideally, Er^{3+} transitions at 1.54 μm could be exploited in wide bandgap semiconductor optoelectronics. As in Er-doped fiber amplifiers, the relevant optical transitions between 4f core states are decoupled from valence interactions, the emission would not be subject to the shifts in performance observed with conventional, temperature-sensitive band-edge optoelectronic semiconductors. Trends observed for Er incorporation in other semiconductor materials have indicated a significant decrease in thermal quenching of PL with increasing band gap, as shown in Figure 1-4.[9,10] Concurrent with this trend, it has also been suggested that the electronic environment provided by more ionic semiconductor hosts enhances the 4f shell Er^{3+} transitions.[5] Michel, et al.,[11] performed impurity co-implantation experiments showing that the presence of light elements dramatically enhance the optical activity of Er in Si. Upon co-implantation of Er and B, C, N and F into Czochralski-grown Si, which has an oxygen impurity background of 10^{18} cm^{-3}, substantial increases in 1.54

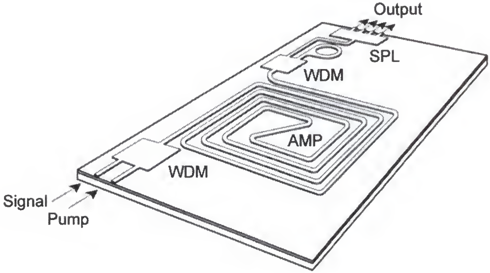

FIGURE 1-3. An integrated multiplexer/demultiplexer and optically-pumped, Er-doped planar waveguide amplifier fabricated on Si developed by G. N. van den Hoven.[4]

μm PL were observed as shown in Figure1-5. Oxygen co-implantation of Er-implanted, float-zone Si, which has an O background of only approximately 10^{18} cm^{-3} and showed very low PL signal without co-implantation, produced erbium luminescence intensity similar to that measured for Czochralski material, It has been theorized that these species alter the local ionic field environment of the Er^{3+} ions, enhancing their optical activity.

Based on these premises, wide bandgap, ionic III-N semiconductors show significant promise as hosts for rare-earth dopants.[13] III-N binary semiconductors and their alloys provide band gap energies ranging from 1.9 eV (InN) to 6.2 eV (AlN). Figure 1-6 displays the relative band gap energies and lattice constants for wurtzitic III-nitrides, some conventional zincblende III-Vs, and Si.[12] As well, the III-N bond is characterized by a strong ionic component compared to other compound semiconductors as can be seen in Table 2.[13] AlN has an electronegativity difference of 1.9 eV and GaN and InN have electronegativity differences of 1.2 eV. In addition, the structural and thermal stability of GaN and AlN make them particularly attractive for reliable, long service-life applications with potential application in extreme environments. Also, GaN LED research has shown that heteroepitaxially grown III-N device materials can demonstrate strong optical activity even when the concentration of structural defects is orders of magnitude higher than that which would severely quench electroluminescence in conventional III-V

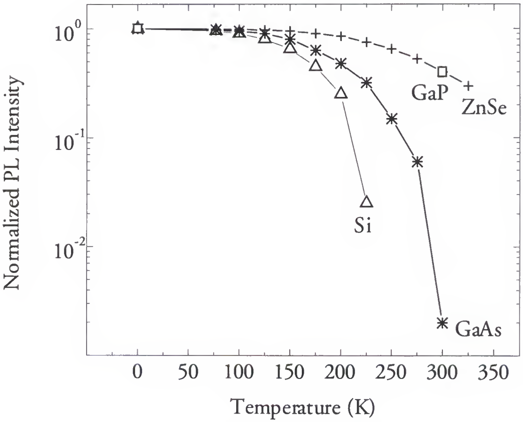

FIGURE 1-4. Thermal quenching of Er^{3+} PL intensity for semiconductors with varying bandgap energies doped with Er by ion implantation (Si, GaAs, and ZnSe[9]; GaP[10]).

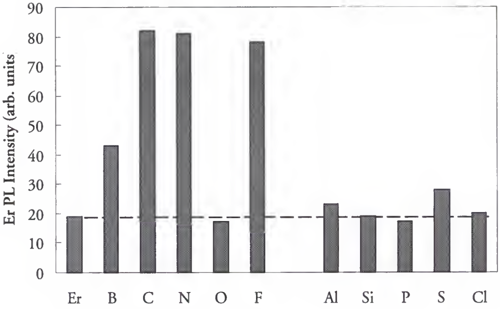

FIGURE 1-5. Erbium PL from implanted, Czochralski-grown Si (except in the case of the O co-implant which was float-zone Si) co-implanted with various elements compared to an Er-doped reference.[11] The Er and co-implant peak concentrations were 10^{18} cm^{-3} in all cases. The O background of the Czochralski Si was ~10^{18} cm^{-3} while the concentration of [O] in the float-zone Si was ~10^{16} cm^{-3}.

semiconductors.[14] This property suggests the possibility of directly integrating III-N:Er materials with Si. In the prior research on erbium in silicon, the presence of light impurities such as carbon and oxygen was seen to have a significant beneficial impact on the 1.54 µm Er^{3+} luminescence. Impurity issues are also important in this work as the III-N have an affinity for carbon and oxygen, both of which have been known to affect the electrical and optical properties of the III-N semiconductors.[15,16]

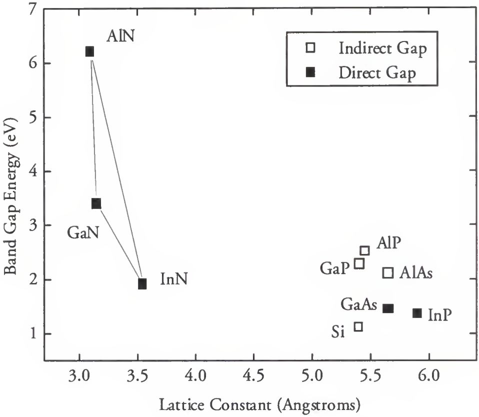

FIGURE 1-6. Band gap energy as a function of lattice constant for the wurtzitic AlGaInN system as well as several zincblende III-V's and Si. Note that the lattice constant used for the III-nitrides is the c-axis parameter. [12]

TABLE 2: ELECTRONEGATIVITY DIFFERENCES
FOR COMPOUND SEMICONDUCTORS

Material	Δ Electronegativity (eV)	Material	Δ Electronegativity (eV)
GaAs	-0.4	InP	-0.4
AlAs	-0.6	GaP	-0.4
InAs	-0.4	AlP	-0.6
ZnSe	-0.9	AlN	-1.4
ZnS	-0.9	GaN	-1.2
CdSe	-0.9	InN	-1.2
ZnTe	-0.4		

In this dissertation, plasma-assisted metalorganic molecular beam epitaxy (MOMBE) techniques have been developed to study Er incorporation and optical activation in III-N semiconductors. Impurity, structural, and activation issues have been studied with the ultimate objective of developing UHV nitride growth from chemical beams to realize 1.54 μm electroluminescence from III-N:Er device materials integrated with Si and to understand some of the optical activation processes in this material.

CHAPTER 2
GROUP III-N GROWTH BY PLASMA-ASSISTED METALORGANIC MOLECULAR BEAM EPITAXY

The introductory section of this chapter discusses the evolution of AlGaInN semiconductor technology and compares some of the III-N growth techniques currently used. The merits of metalorganic molecular beam epitaxy (MOMBE) as a flexible experimental tool are presented. In the later sections, the MOMBE growth aparatus and the materials characterization techniques used in this research will be outlined.

2.1 A Brief History of III-N Research

In the early 1960s, the first GaN researchers recognized the semiconductor's potential for high performance optical and electronic applications.[17] Wide band-gap III-nitrides provided a materials system for optical emitters that could access regions of the visible spectrum, blue and near UV, that had been unobtainable with other III-Vs. As well, AlGaN had the potential for high breakdown, temperature-stable electronic devices for wireless communications electronics and military applications.[18] These extremes in operating parameters were unobtainable with indirect gap Si or other smaller band-gap compound semiconductors such as GaAs and InP. Although the band gap range accessible by the II-VI materials system reached into these higher energy regimes, demonstration of devices with practical lifetimes has been slow due to difficulties in epitaxial growth and structural stability related to the intrinsic physical properties of the II-VI compounds.[12] On the other hand, GaN and AlN couple a wide band gap (3.4 eV and 6.2 eV) with impressive physical and chemical stability. Alloyed with InN, which has a band gap of 1.9 eV, the nitrides can access a range of energies spanning the visible and near UV.

However, the promising capabilities of the nitrides were overshadowed for decades by problems that had proven to be monumental in the development of other wide bandgap materials. High quality epitaxial growth and adequate doping, especially p-type, were largely unobtainable. It has only been in the past several years that GaN and the related InN and AlN have reached the level of a primitive device technology. This has largely been due to the evolution of more advanced semiconductor growth technologies and the determined work of materials researchers. With the evolution of metalorganic chemical vapor deposition (MOCVD) and plasma-assisted molecular beam epitaxy (MBE), GaN of higher structural quality and more controlled defect content became possible.[19,20] This resulted in the achievement of p-type GaN doped with Mg by Amano's group at Nagoya University.[21] Upon that development, the pace of GaN device research accelerated dramatically towards the development of blue LEDs[22] and, more recently, blue lasers.[23-25]

2.2 Metalorganic Molecular Beam Epitaxy of III-N Semicondcutors

Currently, the two most widely researched growth techniques for the deposition of Group III-nitrides have been metalorganic chemical vapor deposition (MOCVD) and molecular beam epitaxy (MBE).[26] However, both of these techniques possess some intrinsic limitations that may affect their applicability to the Group III-nitride system. In order to access band gap energies through the visible range, the ability to deposit high quality In-rich ternaries ($In_xA_{1-x}lN$ and $In_xGa_{1-x}N$) is required. This has been difficult in MOCVD because of the desorption of In at the high growth temperatures required for the decomposition of NH_3. Controllable doping, especially in the case of p-type material, still remains an issue where poor dopant profile control, low activation and hydrogen passivation problems have been significant. Unlike MOCVD, the use of nitrogen plasmas from electron cyclotron resonance (ECR) and radio frequency (RF) sources in ultra-high vaccuum (UHV) allow growth over a wide range of temperatures as the Group V (N) activation mechanism is decoupled from the substrate temperature. The disadvantage facing plasma-assisted MBE is the need to use relatively low growth rates (often < 0.25 μm/hr) in order to achieve acceptable material quality.[26] These low growth rates make growing thick films such as those needed in the epitaxial layer overgrowth schemes used to grow GaN-based laser structures heteroepitaxially on Al_2O_3 very time consuming.[27] Also, UHV techniques cannot take advantage of the scavenging reactions that can occur in the CVD boundary layer that can result in lower impurity backgrounds.[28] Some of the fundamental differences in growth processes for MBE, MOCVD, and MOMBE are depicted in Figure 2-3 (a)-(c).[29] Figures 2-3 (a) and (c) depict the arrival of Group III and Group V species at the substrate from vaccuum where reaction and incorporation take place in MBE and MOMBE. In the case of MOMBE , shown in Figure 2-3 (c), surface reaction is preceded by the cecomposition of alkyl precursors at the growth surface. It is the effeciency of this decomposition and the desorption of its decomposition products that typically dominate the impurity backgrounds of MOMBE-derived films. Figure 2-3 (b) represents the boundary layer-dominated growth front at the substrate/vapor interface in MOCVD. Species in the gas stream are transported to and from

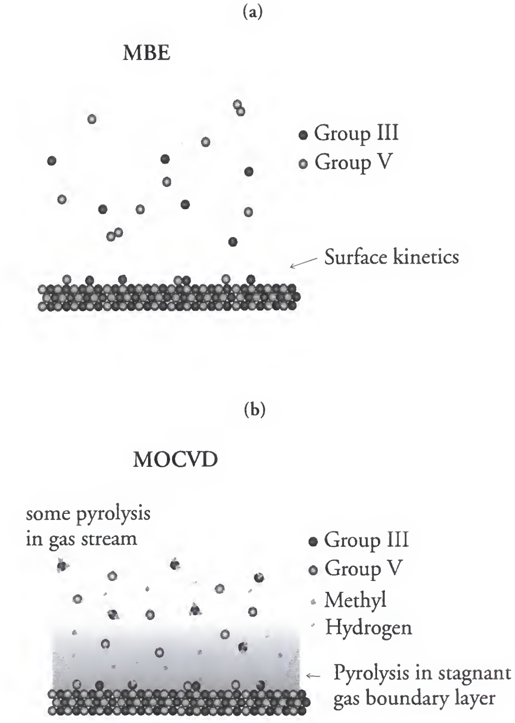

FIGURE 2-3. Idealized surface growth conditions for MBE (a), MOCVD (b), and MO-MBE (c) showing the arrival and decomposition of species at the growth front.[29]

(c)

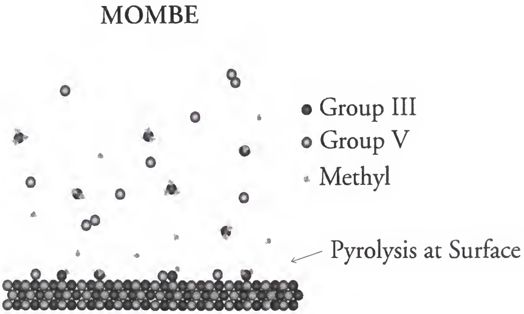

FIGURE 2-3. Continued

the growth surface through diffusion gradients in this stagnant boundary layer that develops at the surface in laminar flow. Prereaction in the gas stream and boundary layer can precede surface reaction while scavenging reactions in the boundary layer can facilitate the passivation and removal of unwanted reaction products and impurities in the source gases.

As in plasma-assisted MBE,[26] the ECR and RF plasma sources available to the MOMBE system allow for low growth temperatures (425°C for the AlN buffer). In addition, MOMBE can take advantage of the high surface mobility of alkyl Group III sources as well as the wide range of dopant and matrix source chemistries available to MOCVD. Unfortunately, with these capabilities come some challenges. Incomplete metalorganic decomposition can lead to low growth efficiencies and high impurity incorporation.

2.3 The Metalorganic Molecular Beam Epitaxy Growth System

In Figure 2-4, a generalized schematic of the MOMBE growth chamber used in this research is shown.[30] Not included in the diagram are the load lock and buffer chambers which are attached to the left of the growth chamber for the orientation depicted in Figure 2-4. These vaccum compartments, linked by a substrate-block magnetic trolley system, provide a means of loading several substrates into the system while maintaining growth chamber vaccuum and minimizing the communication of unwanted species from the room atmosphere to the deposition environment and vice versa. Using a transfer arm, substrate blocks can be taken from the buffer chamber and placed onto the radiative heater assembly in the growth chamber through a large gate-valve orifice. Generally, growth experiments are conducted on 2" substrates although 3" susbtrate blocks are available. Smaller substrate pieces of non-uniform shape can be In-mounted to 2" Si backing wafers and loaded into the standard susbtrate blocks. Since the heating mechanism relies on the absorption of radiation by the substrate, transparent substrates must be supplied with a backside absorber in intimate thermal contact. For temperatures less than approximately 800°C this can be achieved through In-mounting transparent substrates such as sapphire to Si backing wafers. However, as substrate temperature increases loss of In leads to poor thermal transfer between mounting wafer and substrate. For growth on sapphire at high temperatures or where a high degree of thermal uniformity across the substrate is desired, substrates are backside-coated with a 10 μm low pressure chemical vapor-deposited polysilicon film which acts as an efficient absorption layer in intimate thermal contact with the substrate.

Once a substrate block is fixed to the substrate heater through a locking-pin system and the growth chamber is isolated from the buffer chamber, the block can be flipped into the growth position facing the injectors and sources. During growth the substrate block is continuously rotated at a rate of approximately 15 revolutions per minute to achieve uniform deposition from the molecular beam sources which are aimed at an angle to the substrate surface normal. Substrate temperature can be monitored by a thermocouple bonded to a Si chip which is permanently mounted between the radiative heating coils and the substrate block. Also, the temperature of the substrate surface can be measured more directly by optical pyrometry through a transparent viewport which is aligned in the center fo the source flange facing the substrate block assembly. Temperature calibration of different substrate materials and configurations can be approximated by the use of portions of materials with a distinct and easily observable melting point. Pieces of crystals such as InSb and GaSb are mounted to silicon backing wafers and slowly heated through their melting point while being observed through a substrate-looking viewport. The melting temperature ob-

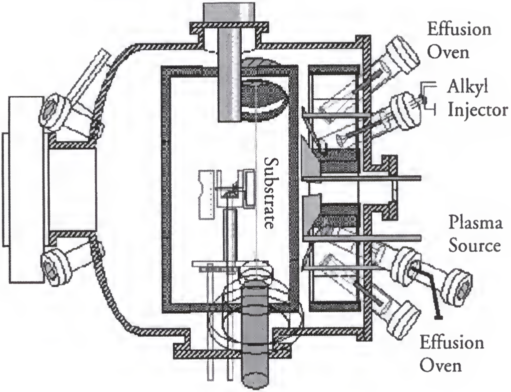

FIGURE 2-4. A generalized schematice of the MOMBE growth chamber (adapted from a diagram by Paul van der Wagt).[30]

served with the thermocouple can then be correlated with the material's actual melting point to calibrate the thermal characteristics of that particular substrate configuration.

As indicated on the right side of the diagram, several different types of matrix and dopant molecular beam sources are available. These include thermal effusion ovens for elemental source doping and matrix components such as Er, Ga, In, and Sb. The effusion ovens are relatively simple to operate and maintain and provide all of the growth capabilities of conventional MBE. They also possess the drawbacks of MBE systems such as limited growth chemistries, poor growth uniformity with substrate scale-up, oval defects, and lengthy restocking procedures which require venting of the growth chamber to atmosphere. There are also two types of gas injectors mounted on the source flange. The alkyl injectors allow the controlled introduction of beams of carrier gas-borne metalorganic precursors into the growth chamber. These injectors can be easily scaled-up as they utilize multiple-hole effusion plates which overcome the single point-source geometry that limits effusion oven uniformity. The vent-run switching of the metalorganic-bearing carrier gas allows for abrupt and stable growth initiation and doping profiles. The metalorganic source compounds are contained in stainless-steel bubblers and transported to the injectors by a mass-flow-controlled carrier gas, such as He or H_2, through stainless steel lines. A wide dynamic range of molecular source fluxes from metalorganic compounds with thermally dependent vapor pressures can be obtained by controlling the bath temperature, bubbler outlet pressure, and carrier gas flow rates. A diagram of the bubbler and controller systems is shown in Figure 2-5. The upstream placement of the mass flow controller prevents decomposition of precursor molecules in the heated convection sensors in the controller. Source vapor pressures are typically a few Torr at 10° to 20° C. By varying the outlet pressure, metalorganic uptake

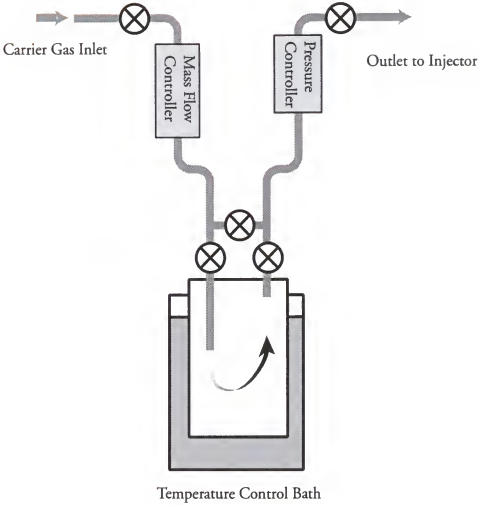

FIGURE 2-5. Configuration of a metalorganic source module composed of bubbler, transport and control elements.

by the carrier gas can be controlled over nearly two orders of magnitude. Typical carrier gas flow rates range from 1 to 10 sccm. Since, the metalorganic bubblers are housed in an external manifold cabinet, restocking or changing sources does not require venting of the growth chamber. Special care must be taken to run n- and p-type dopants and certain In and Al precursors through separate injectors to prevent residual compensation and alkyl exchange in the injector which can dramatically reduce growth efficieny. In general, the injectors are heated to 65°-100° to prevent condensation of metalorganics or other background impurities from the growth chamber on the injector components. In the case of some low vapor-pressure sources, the stainless-steel supply lines must be heated to prevent condensation of the metalorganic in the lines before reaching the injector.

The source flange also has hydride injectors for the introduction of Group V and Group IV species like AsH_3, PH_3, and SiH_4. A catalytic thermal-cracker element is incorporated into the injector which decomposes the hydride molecules into reactive growth species. The hydrides, particularly AsH_3, are extremely toxic and necessitate numerous safeguards, safety procedures, and extreme care on the part of all laboratory personnel. It is the toxicities of these compounds that define the safety envelope of practices and equipment in the MOMBE laboratory. All gas supply lines run in evacuated conduit which, along with the exhausts of all pumps and vent lines that could possibly be exposed to the hydrides, are exhausted after passing through multiple scrubber stages. A redundant, multi-point toxic gas detection system constantly monitors the air at various points in and around the growth system, transport lines, and source storage cabinets. Anytime that maintenance procedures require the exposure of the internal surfaces of the growth chamber, transport lines, or pumps on the growth chamber, self-contained breathing aparati (SCBA) are worn. Various interlock systems can shutdown process valves and vaccuum valves in the event of a loss of power or exhaust system failure to prevent any release of toxic gas.

Finally, the MOMBE system can be fitted with electron cyclotron resonance (ECR) and radio-frequency (RF) plasma cells that can be used to produce activated species of otherwise unreactive precursors such as ground-state molecular nitrogen for growth of III-nitrides or hydrogen for substrate cleaning.

The RF source generates a plasma by directly coupling 200-600 Watts of RF energy into the source's plasma chamber which is fed gas species through a mass flow-controller. In

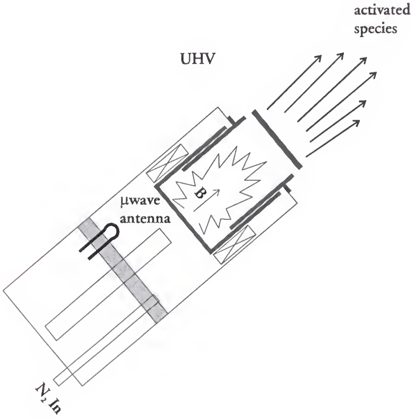

FIGURE 2-6. ECR plasma source diagram based on the Wavemat MPDR 610.

the plasma chamber, the RF energy ionizes the source gas creating an intense plasma composed of a distribution of atomic and molecular species which can escape into the growth chamber as a chemical beam directed at the substrate through an orifice. The ECR power supply generates microwave energy at a frequency of 2.45 GHz. This energy, typically supplied at rates of 150-300 Watts, is guided into the source chamber where it is coupled into the electron cloud from the ionized plasma. A series of permanent magnets around the source creates a magnetic field along the axis of the plasma chamber as shown in Figure 2-6. This field accelerates the electron motion induced by the microwave excitation into helical paths which collide with and ionize the source gas molecules, efficiently creating a dense plasma. Plasma species can then effuse out of the open end of the source tube, covered by a biasing grid, into the vaccuum of the growth chamber, forming a beam which is directed toward the susbtrate. The grid provides a means to accelerate or decelerate ions effusing out of the plasma source.

2.4 Vaccuum Systems

When considering growth techniques it is natural to focus on the capabilities of the components within the growth chamber. The MOMBE system's combination of alkyl injectors, hydride injectors, effusion cells, and plasma sources allow it to grow an unrivalled diversity of electronic and photonic materials. Yet, the true foundation of the system resides in the pumping systems that are able to keep the growth chamber in the molecular flow regime while fluxes of reactive and pyrophoric metalorganics, toxic hydrides, carrier gases, and plasma streams are being continuously fedinto the chamber. And, it is the maintenance

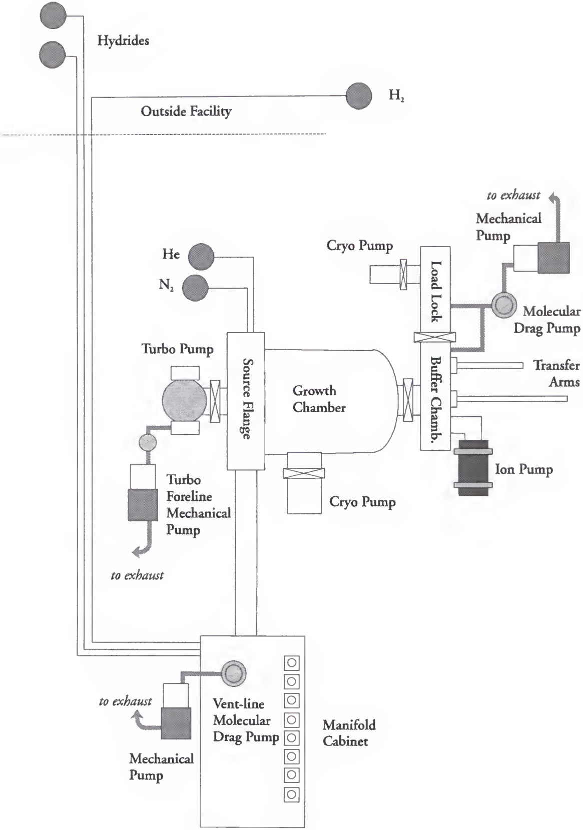

FIGURE 2-7. Schematic of the MOMBE system including transfer chambers, gas supply and vaccuum hardware.

and care of these pumping systems that rank among the most critical and most challenging responsibilities in the MOMBE laboratory.

A schematic of the growth system, supply gases, and vaccuum hardware is displayed in Figure 2-7. A dual rotor, 2200 liter/second Balzers turbo pump is at the heart of the system. During growth, the turbo pump is assisted by a CTI-8 cryopump which is very effective at pumping larger molecular-weight organics and organic fragments such as the ever present ethylene and methane leaving groups. In complementary fashion, the turbo pump is able to pump He, the most commonly used carrier gas, which the closed-cycle He refridgerator-based cryopump cannot. Also, an extensive LN_2 cryoshroud system assists the turbo and cryopumps during growth, minimizing the evaporation of unwanted species onto the substrate from chamber surfaces facing the substrate, especially the source flange which can contain any number of sources at elevated temperatures. The turbo pump is backed by a mechanical pump lubricated with hydride-compatible perflourinated ethers. The mechanical pump and the enclosed air spaces around it, the bubbler modules, the source flange, and the process lines are exhausted to a high-volume toxic scrubber system. This facility scrubber system has a diesel generator-based emergency power system that is automatically activated if electrical service is lost. Immediately following any exposure to the atmosphere, the entire growth chamber is heated in an insulating enclosure to temperatures reaching 150-200 °C. The primary purpose of this baking procedure is to drive water out of the chamber walls absorbed while the chamber was vented. The system is also baked immediately prior to venting the system to atmosphere in order to drive off any residual metalorganics or other toxics as a safety precaution. Generally the growth chamber pressure is less than 10^{-8} Torr immediately following a bake cycle. During growth, pressures can rise to10^{-5}-10^{-4} Torr depending on the amount of gas flowing into the chamber.

The buffer chamber is evacuated by an ion pump which, in the absence of freshly transfered substrate blocks from the growth chamber or the load-lock, maintains the buffer chamber pressure below 10^{-8} Torr. The load lock, after roughing, is pumped to pressures of 10^{-7}-10^{-8} Torr with a CT100 cryo-pump which shoulders the important task of adsorbing, among other species, any water molecules out-gassing from newly-loaded substrate blocks. The load lock and the growth chamber are roughed from atmosphere to the 10^{-4} Torr regime with a molecular drag pump backed by a mechanical pump. This roughing system is exhausted to the aforementioned facility scrubber system.

2.5 General Growth Procedures

This section outlines a typical MOMBE III-N growth run. Where the growth experiments presented in the following chapters differ from this general sequence, it will be contextually noted there. A growth run begins with the preparation of a substrate or batch of substrates. The primary substrates used in this research were 2"-diameter, (0001) Al_2O_3, commonly referred to as 'c-plane' sapphire, and (001) Si. However, growth experiments were conducted with a number of other substrates to evaluate there feasibility, including: GaAs, ZnO, $LiGaO_2$, and $LiAlO_2$.[31] As mentioned in section 2.3, transparent substrates must be supplied with an absorptive backing. This is done by either manually In-mounting the substrate to a backing wafer. usually Si, on a hot plate or by having substrates backside-coated with a 10 μm polysilicon film using low-pressur chemical vapor deposition. All polysilicon backside-coated sapphire substrates used in this work were processed, per the author's specifications, by Union Carbide Corporation - Crystal Products Division. Any substrate pieces smaller than 2" had to be In-mounted to a 2" Si wafer or a solid-faced Mo subtrate block. In addition, In-mounting of several smaller susbtrate pieces on a single Si backing wafer made it possible to conduct comparitive experiments with different substrates under identical growth conditions. Generally, epi-ready sapphire substrates were removed from their clean room-packed wafer holders, mounted, and directly entered into the load-lock chamber. Where growth on Si was being conducted, substrates were mounted, if necessary, cleaned with a 60 second buffered oxide etch and a 60 second de-ionized water rinse and immediately loaded into the load -lock chamber.

After intiating the the load-lock evacuation process, all thermal elements to be used during the growth run were outgased by heating them5-10% over their final operating temperature for that particular experiment in order to drive off any adsorbed or absorbed impurities. This includes effusion ovens, injectors, and the substrate heater. Also, at this time RF or ECR power and flow were applied to the plasma source and a plasma was ignited in order to drive-off any impurities adhered to the plasma chamber. This heatup procedure was conducted with LN_2 already in the cryoshroud panels. When the load-lock pressure reached approximately 10^{-6} Torr, The substrate block trolley was transferred to the buffer chamber. After the effusion sources and injectors equilibrated back at their operating temperatures, the substrate was transfered from the trolley onto the substrate heater assembly in the growth chamber. During the substrate block transfer process, the plasma was momentarily extinguished and the N_2 flow to the source interrupted to prevent back flow of significant amounts of gas into the buffer chamber. After isolation of the buffer and growth chambers, the plasma was re-ignited. Then, the substrate was flipped into the growth position and ramped up to 700°C under plasma exposure. This was performed in order to blow off any adsorbed species on the surface and to nitride the sapphire surface, providing a template for subsequent III-N growth. At this time, flow was established through the metalorganic bubblers into the vent line.

After cooling the substrate down to 425 °C, the Al source was switched from the vent line into the injector to deposit a 300 Å AlN buffer layer on the sapphire substrate. The utility of such buffer layers has been observed in MBE and MOCVD of GaN. MOMBE-derived AlN deposited at low temepratures has been shown to be an excellent buffer layer for subsequent AlN and GaN growth throughout this research. Atomic force microscopy has indicated a surface roughness of less than 10 Å for thin, low temperature AlN buffer layers and subsequent thick layers (9000 Å).[32] Upon completion of the buffer layer, the

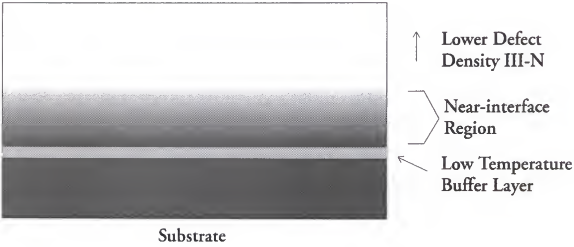

Figure 2-8. Idealized III-N film cross-section showing the defective region near the substrate/film interface

substrate was heated to the final growth temperature, and the appropriate Group III source was switched into the chamber, commencing growth. If this experiment was to involve optical or electrical dopants, any doped layers would generally be preceded by a few thousand Angstroms of undoped material. This spacer layer serves to remove the active layers of interest from the high density of impurities and structural defects often found immediately following the intitial substrate-film growth interface as shown in Figure 2-8.

2.6 Characterization

Materials characterizaion is a fundamental part of this dissertation research. Techniques including atomic force microscopy (AFM), scanning and transmission electron microscopy (SEM and TEM), high resolution x-ray diffraction (HRXRD), secondary ion mass spectrometry (SIMS), Auger electron spectroscopy (AES), optical spectrophotometry, cathodoluminescence, and laser photoluminescence (PL) have been employed in this work to understand the growth and optical activation of this new class of III-N:Er semiconductor materials.

Atomic force microscopy was performed with a Digital Instruments Nanoscope III. The AFM was operated in tapping mode. X-ray diffraction studies of structural quality were performed with a Philips MRD system. This system, represented in Figure 2-9 combines a 4-crystal monochromator/collimator and a post-sample monochromator before the detector. This precise limting of the incident and diffracted x-ray beams allows the separation of peak-broadening effects. Fixing the detector angle (2θ) and varying the incident angle (Ω) maps the shape of the Bragg reflection selected by the fixed sample-to-detector angle. The width of this peak depends directly on sample mosaicity, microtilts and structural perturba-

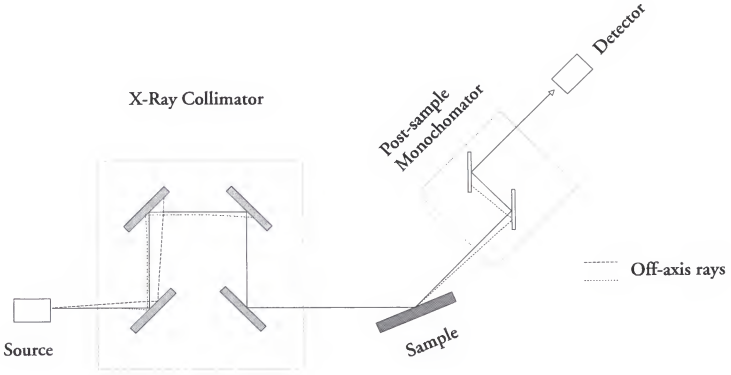

Figure 2-9. Generalized schematic of the high resolution x-ray diffraction system.

tions which reflect the structural quality of the epitaxial layer. Operating in the symmetric mode, where both the incidence angle Ω (or θ) and the sample-to-detector angle 2θ are varied, produces an x-ray rocking curve for which the full width at half-maximum (FWHM) primarily reflects the lattice constant distribution. Structural quality was also characterized using electron microscopy. Scanning electron microscopy was performed with a JEOL 35 CF. SEM's utility for observing morphology results from its large depth of field. Transmission electron microscopy, using the wave-like nature of electrons, allowed for selected area diffraction patterns that reflect the epitaxial quality of crystal films and allow for the verification of the film/substrate epitaxial orientation as in Chapter 3. TEM work was performed by Sushil Bharatan, Brent Gila and V. Krishnamoorthy.

Auger electron spectroscopy was performed with a Phi scanning AES system under the direction of Eric Lambers at the MAIC facility. AES is a very sensitive technique that can provide compositional information with a few nanometers of the surface. Electrons relaxing to core levels ionized by the incident 10-20 keV electron beam cause the ejection of lower energy Auger electrons. Due to their relatively low energy (10^2 meV scale) only Auger electrons with a few nanometers of the surface can escape to be detected. The escaping Auger electrons are then analyzed and the energy spectra observed is compared with standards and Auger energy tables to determiine the elemental make-up of the near surface region. The Auger is equipped with an ion gun which is used to sputter away the sample. Alternating sputtering and Auger surface scans can be performed to produce a composition-depth profile.

Secondary ion mass spectrometry, performed by Dr. Robert Wilson at the Charles Evans and Associates facility, was used to study dopant and impurity content and distribution in the III-N films grown in this work. In this technique, species sputtered from the sample surface with a

Cs or O ion beam are analyzed with a quadropole mass spectrometer. In this way concentrations of impurities and dopants can be measured, with the assistance of reference standards, levels as low as 10^{15} cm^{-3}.

Laser-induced photoluminescence was perfomed to probe the optical activity of Er^{3+} in III-N hosts. The earliest PL data for AlN:Er was collected by Dr. Robert Schwartz at Hughes Laboratories in Malibu, California. Later photoluminescence characterization, including temperature dependent and luminescence lifetime measurements from AlN:Er and GaN:Er were performed by Uwe Hommerich, Myo Thaik, and J. T. Seo at Hampton University and by the author at the University of Florida. Spectral photoluminescence tequniques use a grating spectrometer and an InGaAs or Ge detector to measure laser-induced emission from the sample. Luminescence decay measurements are made with high speed detectors. An Ar ion laser was used as the pump source. Photoluminescence thermal-quenching measurements were conducted with the use of a He cryostat capable of temperatures of cooling samples to ~8 K.

The optical absorption spectra presented in Chapter 3 were collected using a Cary 14 UV-vis spectrophotometer under the direction of Prof. Jon Stewart, Department of Chemistry, University of Florida. This device passes light of a selected wavelength through a sample and measures the transmitted signal. This signal is then compared to that from a reference blank to determine the absorption spectra of the film under study.

Cathodoluminescence studies of Er^{3+} activation were conducted at the Ohio State University by Leonard J. Brillson and his group. In this technique, electron beam-induced emission from III-N:Er samples produced visible and IR emission spectra that reflect a range of excitations including above -bandgap and sub-band direct Er excitation. By varying the acceleration voltage of the electron beam, depth profiling of the luminescence is possible.

CHAPTER 3
OPTIMIZATION OF III-N GROWTH BY PLASMA-ASSISTED METALORGANIC MOLECULAR BEAM EPITAXY

Naturally, a semiconductor device technology must be developed upon a basis of understanding of the fundamental growth issues rellevant to producing high quality materials. In the following sections of this chapter the optimization of various aspects of plasma-assisted metalorganic molecular beam epitaxy (MOMBE) of III-N semiconductors will be discussed including growth temperature, plasma conditions, and substrate material. Since the Group V flux is such a critical issue in ultra high vacuum growth of III-N materials, a focused series of experiments on optimizing the nitrogen plasmaconditions is presented in a separate section of this chapter. Conspicuous in every section of this experimental work is the understanding and control of impurities and defects. Plasma-assisted MOMBE has been shown to be an effective tool for III-N growth research and a technique capable of producing materials of sufficient quality to establish a foundation for the investigation of III-N:Er optoelectronics.

3.1 An Optimization Study of Metalorganic Molecular Beam Epitaxy of Aluminum Nitride and Gallium Nitride Semiconductors

This section has established the basic capabilities of plasma-assisted MOMBE for growing AlN and GaN. The experiments here have also sought to optimize materials quality through the controlled variation of process parameters.[33] Several metalorganic Group III

TABLE 3-1: RELATIVE GROWTH EFFICIENCIES OF CONVENTIONAL III-V AND III-N MATERIALS BY MOMBE

Group III Source	$G_{\text{nitride}} / G_{\text{IIIAs,IIIP}}$
dimethylethylamine alane	1.0
trimethylamine alane	1.0
triethylindium	0.80
trimethylindium	0.41
triisobutylgallium	0.23
triethylgallium	0.56
trimethylgallium	0.12

sources commonly used in MOMBE and metalorganic chemical vapor deposition (MOCVD) were employed to grow III-N films. Table 3-1 shows the growth rates of III-N materials as compared to III-As or III-P films grown with the same Group III flux. The generally lower growth efficiencies for the nitrides, except for trimethylamine alane (TMAA) can be attributed, as in the antimonides, to the less catalytic nature of the nitrogen stabilized surface relative to a P- or As-rich surface.[34]

Dramatic differences in the impurity backgrounds were seen in AlN samples grown with TMAA compared to dimethylethylamine alane (DMEAA). A substantial decrease in the C (from ~10^{21} cm^{-3} to ~10^{20} cm^{-3}) and O (from ~10^{20} cm^{-3} to ~10^{18} cm^{-3}) concentrations as determined by SIMS was observed in the DMEAA grown material. The molecular structures of TMAA and DMEAA are shown in Figure 3-1. This drop in impurity levels is

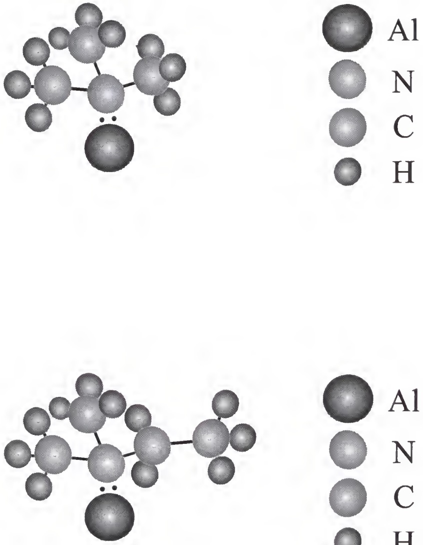

FIGURE 3-1. Molecular structures of trimethylamine alane (top) and dimethylethylamine alane. The substitution of the ethyl group in the dimethethylamine alane changes the solubility of the compound allowing for etherless liquid processing.

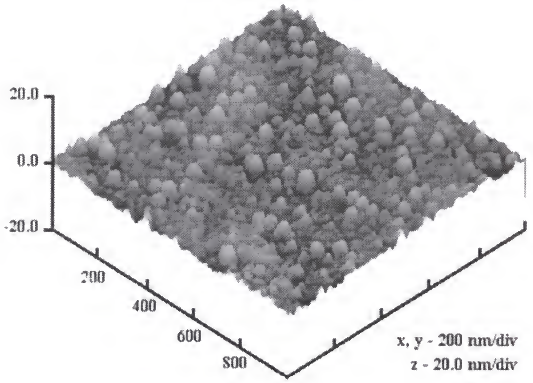

FIGURE 3-2. Tapping mode AFM surface image of a 9000 Å DMEAA-derived AlN film preceded by an AlN low temperature buffer on (0001) Al_2O_3. The RMS roughness calculated for this surface was < 8 Å.

likely due the absence of ether, which is required in the processing of the solid trimethylamine alane. Using DMEAA and an ECR nitrogen plasma, a root mean square (RMS) roughness of <8 Å, as determined by atomic forcce microscopy, was achieved. This surface indicates a planarization of the substrate which showed an RMS roughness of approximately 14 Å. The tapping-mode surface scan is presented in Figure 3-2. Transmission electron microscopy indicated that the DMEAA-derived AlN on sapphire was epitaxial with the (0001) axis of AlN parallel to the (0001) Al_2O_3 axis. This can be seen in the selected area diffraction pattern imaged from a region near the AlN/sapphire interface shown in Figure 3-3.[32] The well-defined diffraction spots from the hexagonal AlN fall within the corresponding spots

FIGURE 3-3. Selected area diffraction pattern taken with TEM near the interface of a DMEAA-derived AlN film and the (0001) Al_2O_3 substrate.

of the Al_2O_3 pattern along the same symmetry lines. The absence of circular distortion of the AlN diffraction spot shape indicates that the AlN and the low temperature buffer have grown with a strong epitaxial coherence to the substrate. The good structural quality of these films was indicated by a 430 arc-second W-scan X-ray rocking curve full-width at half maximum (FWHM) as can be seen in Figure 3-4.

Having demonstrated the high quality growth of AlN on sapphire by plasma-assisted MOMBE, the experimental focus was turned to GaN. Although GaN does not have as large a band gap as AlN, it is of more immediate technological interest because it can be doped electrically. A series of growth experiments were conducted to determine the optimum

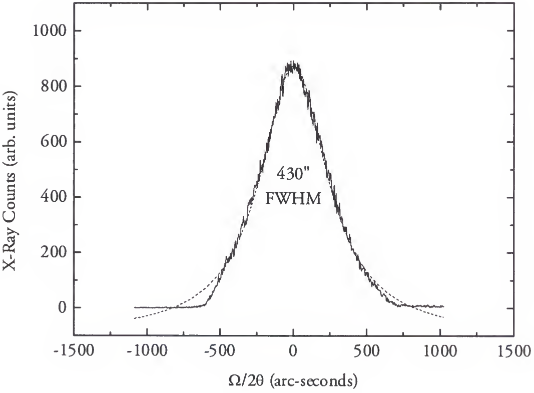

FIGURE 3-4. ΔΩ X-ray rocking curve from MOMBE AlN grown on (0001) sapphire.

conditions for depositing epitaxial GaN by plasma-assisted MOMBE. Structural quality, surface morphology and interband absorption were correlated to growth tempera- A fourfold drop in Ω-scan X-ray rocking curve FWHM, depicted in Figure 3-5 was observed for ~1 µm layers grown at substrate temperatures from 625 °C to 925 °C. Growth rates varied little over this temperature range (4500 - 4000 Å/hour), suggesting neither Ga desorption nor reactive Group V surface concentration were rate limiting factors.

A similar trend to that observed in structural quality was also seen in the UV/VIS optical absorption behavior as measured by a Cary 14 spectrophotometer. For samples grown at lower temperatures, a strong interband absorption tail was observed in the absorption spectra similar to the 2.3 - 2.7 eV feature observed in plasma-assisted MBE and MOCVD

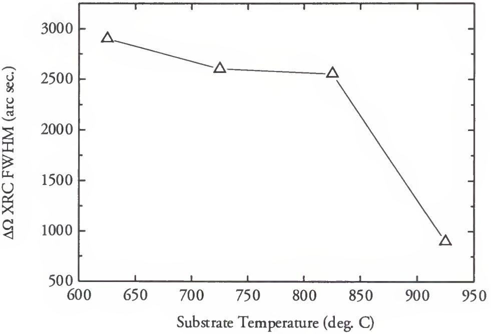

FIGURE 3-5. **ΔΩ X-ray rocking curve peak widths of 1 µm GaN films as a function of substrate temperature.**

material.[35,36] Absorption spectra measured for GaN films grown at two different temperatures and sets of ECR plasma parameters is shown in Figure 3-6. The interband absorption feature decreased monotonically with increasing temperature as can be seen in Figure 3-7. Numerical fitting of the temperature dependence of the absorption coefficient measured at 2.9 eV indicated that the removal or deactivation of the optically active center responsible for this interband absorption followed an Avrahmi-type thermal activation energy of approximately 110 meV.

Surface roughness of TEGa-derived GaN/Al_2O_3 as quantified by AFM also showed a significant temperature dependence as shown in Figure 3-8 where a peak in RMS surface roughness was observed in samples deposited at 825 °C. The reductions in roughness at higher temperatures corresponded with the improvements in the structural quality as characterized in the x-ray data. This further supports the trend toward high quality epitaxial growth at elevated temperatures. The planarization at low substrate temperatures may represent a low surface-mobility, planar growth mode approaching the regime exploited in low temperature buffer layers.

This optimization study of TEGa/ECR N GaN has demonstrated that high quality material can be grown by MOMBE. However, growth rates for the practical fabrication of thick layers still remain an issue for UHV techniques, particularly if thick layers are needed to maximize structural quality near the active device layers. Figure 3-9 shows the high resolution x-ray diffractions rocking curves of the (0002) GaN reflection for a 4 μm layer grown at ~ 5000 Å/hr using the optimum conditions described above. High resolution 5 crystal x-ray analysis with the use of a detector monochromator allows the precise separation of peak broadening effects as described in Chapter 2. Fixing the detector angle (2θ) and

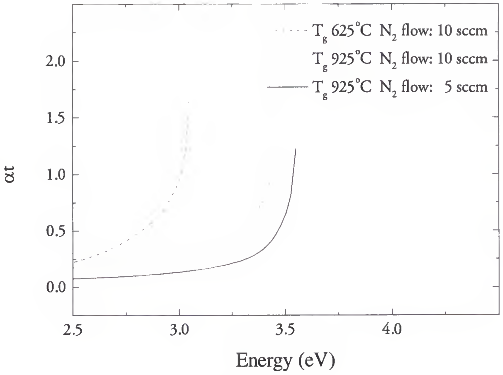

FIGURE 3-6. Spectrophotmeter absorption spectra from 1 μm GaN films grown under varying process parameters.

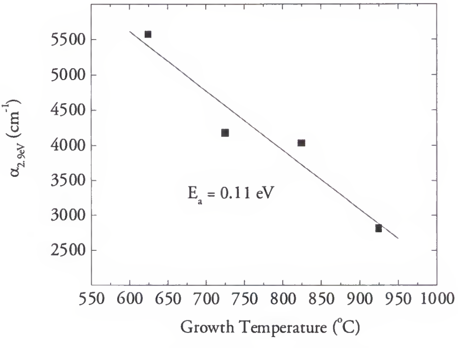

FIGURE 3-7. Absorption coefficient at 1.9 eV from 1 μm GaN films plotted as a function of substrate temperature. Fitting the data to an Avrahmi-type exponential, gives an activation energy of approximately 110 meV.

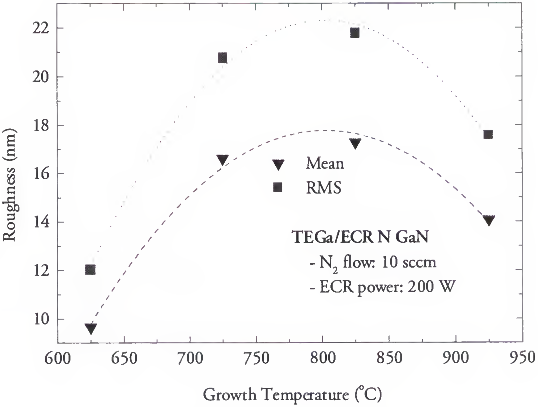

FIGURE 3-8. **Atomic force microscopy-determined surface roughness of 1 μm GaN films plotted as a function of substrate temperature.**

varying the incident angle (Ω) maps the shape of the Bragg reflection. The width of this peak depends directly on sample mosaicity, micro-tilts and structural perturbations which reflect the structural quality of the epitaxial layer. Operating in the symmetric mode, where both the incidence angle Ω (or θ) and the detector angle 2θ are varied, produces an x-ray curve for which the full width at half-maximum (FWHM) primarily reflects the variation in lattice constant. An Ω scan x-ray FWHM of 6.8 arc-minutes and an Ω/2θ FWHM of 42 arc-seconds was measured for the 4 μm GaN sample. This shows an improvement in FWHM as compared to peak widths from 1 μm samples grown under the same conditions

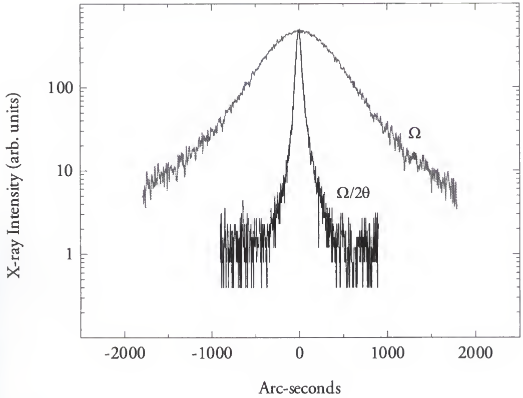

FIGURE 3-9. High resolution x-ray rocking curves from a 4 μm GaN film showing Ω and Ω/2θ scans of the (0002) reflection.

where we measured an Ω peak width of 9.6 arc-minutes and an $\Omega/2\theta$ FWHM of 48 arc-secs. This GaN film thickness correlation with X-ray FWHM follows a general trend that can be seen in Figure 3-10 where some of the best FWHM values reported in the literature[37-41] are plotted along with the data from the MOMBE-derived GaN grown on Al_2O_3 developed in this dissertation. In terms of structural quality, the plasma-assisted MOMBE GaN samples from this study are quite competitive with materials grown by plasma-assisted MBE and MOCVD.

During the growth experiments with GaN dramatic changes in the quality of ECR plasma-derived GaN by were brought about by varying the growth parameters. However, the growth rate varied little. This is particularly interesting in the case of lowering the N_2 flow into the ECR source, especially at high temperatures where Group V desorption would be accelerated. Decoupling of growth from the effective V/III ratio suggests that the abundance of reactive nitrogen species at the growth surface does not limit the growth rate of high quality material. This supports the premise that epitaxial growth may be controlled by the surface mobility of reactive nitrogen species. If the nitrogen surface mobility can be increased by weakly binding the N to a ligand such as iso-butyl or t-butyl, it may be possible to increase the growth rate without degrading the crystallinity. To investigate this, experimentation with two gaseous nitrogen precursors, tertiarybutyl amine and tri-isobutyl amine was conducted. Unfortunately, though growth of AlN from both precursors was achieved, growth of GaN without the presence of significant Ga-metal droplet formation was not possible under any growth conditions, presumably due to poor pyrolysis of the nitrogen precursors. In addition, the AlN films deposited from these sources possessed high impurity backgrounds and poor structural and optical properties for a wide range of source fluxes.

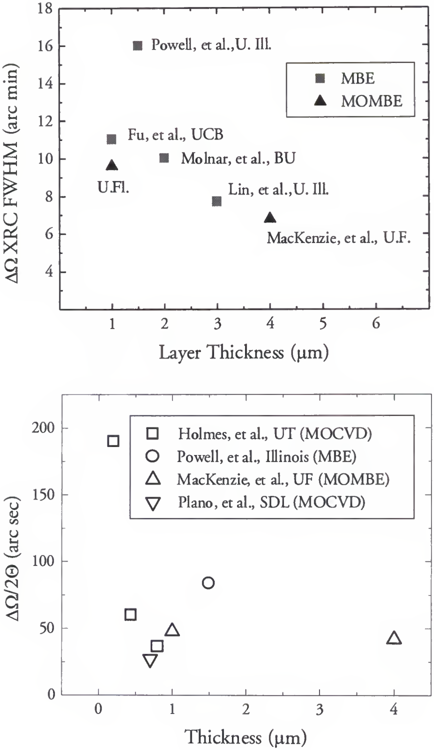

FIGURE 3-10. **High resolution x-ray FWHM data for GaN films grown by several techniques plotted as a function of layer thickness.**

Films were deeply amber in color as compared to the transparent appearance of plasma nitrogen-derived AlN. The (0002) x-ray reflections from the nitrogen precursor-derived films was too broad and weak to be analyzed with high resolution x-ray diffraction. Thus, it does not appear that carbon-bonded nitrogen sources will be suitable alternatives to plasma-activated nitrogen.

In conclusion of this section, the high-quality growth of AlN and GaN by plasma-assisted MOMBE has been demonstrated . A substantial reduction in C and O backgrounds was observed in AlN grown with the liquid DMEAA as compared to AlN grown with TMAA. TEGa proved to be the best precursor for GaN and the optimization experiments conducted in this work determined that high growth temperatures (925 °C), lower V/III ratio (5 sccm N_2) and 200 W ECR power produced the highest quality films in terms of structural quality, surface morphology and minimized interband absorption. Experimentation with the alternative nitrogen sources suggested that a non-carbon bonded nitrogen precursor may be required for high quality growth.

3.2 Alternative Oxide Substrates for III-N Heteroepitaxy

The range of commercially-available substrates available for use in III-nitride epitaxy is limited. While small quantities of GaN substrate materials are being produced in experimental batches, they are not yet commercially available in quantity. The most commonly used substrate for growth of nitride devices to date has been sapphire, which has a large lattice mismatch to the nitrides. In addition to the high defect densities, sapphire also requires the use of low temperature, and hence typically high resistivity, nucleation layers. Typically, GaN-based device structures include a thick (several μm) spacer layer between the defective sapphire interface and the active regions. Recently, growth strategies such as epitaxial layer overgrowth have been utilized to create low defect areas in GaN films by laterally off-setting these areas from high densities of defects threading up from the substrate interface. However, the usable wafer area using such growth schemes is limited. Coupled with the high resistivity of sapphire, low resistance ohmic contact formation is complicated by the need to process lateral rather than backside contact geometries as normally used for fabrication of other vertical-architecture III-V photonic device structures. Wurtzitic SiC offers a significant improvement in mismatch, as can be seen in Figure 3-11, though true lattice-matching is still not possible. Furthermore, the cost is still prohibitively high for substrates of reasonable quality and size. SiC substrate pricing is generally on the order of \$$10^3$ per square centimeter while (0001) sapphire is available for less than \$10 per cm^2 from a number of vendors. In terms of lattice constant, ZnO is a more attractive alternative for growth of GaN,[42-45] even allowing for lattice matching at the appropriate compositions of $In_xGa_{1-x}N$ or $In_xAl_{1-x}N$. This material is presently available in sizes up to one inch though surface finish and material quality are still under development. The newest candidates for use in III-nitride epitaxy are the oxides $LiGaO_2$ and $LiAlO_2$. These materials also offer the prospect of true lattice matched epitaxy. There are lattice matches for a range of AlGaInN mixtures for the gallate and the aluminate. Unlike ZnO and SiC, these materials can be grown by Czochralski making their scaleup to large diameters more feasible in principle than for ZnO.[46] It is also hoped that because they are closely matched to the nitrides, low temperature nucleation layers will not be required. Preliminary results from growth of GaN by MBE[47] and MOCVD are quite encouraging, with defect densities reportedly less than 10^7 cm^{-2}. However, to date, little information is available about the nucleation behavior on these novel oxide substrates,

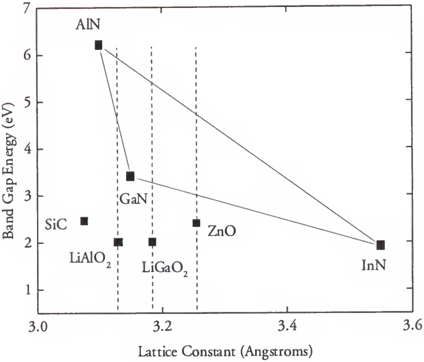

FIGURE 3-11. Band gap as a function of lattice constant for the III-N semicondcutors and other closely-matched potential substrate materials

particularly when using gaseous precursors in ultra high vacuum. This section represents a preliminary evaluation of the growth of III-N films from metalorganic sources in UHV on these alternative oxide substrates.

Group III-nitride layers were grown on oxide or GaAs substrates In-mounted to Si backing wafers using an Intevac Gas Source Gen II MOMBE system as described in Chapter 2. Square ZnO substrates, ~ 0.25 - 1 cm^2, were obtained from Litton Inc.. 2" diameter epi-ready sapphire substrates from Union Carbide and 2" diameter SI GaAs were cleaved into approximately 1 cm^2 pieces and In-mounted on Si simultaneously with the ZnO for comparison of growth under identical conditions. Films on ZnO and $LiGaO_2$ were grown under a reactive nitrogen flux provided by an Electron Cyclotron Resonance (ECR) plasma source (Wavemat MPDR 610) operating at 2.45 GHz and 200W forward power. Layers grown on $LiAlO_2$ were grown using an RF plasma at 2-4 sccm nitrogen and 350-450W. The aluminum source was dimethylethylamine alane (DMEAA). The gallium source was triethylgallium (TEGa). And, trimethylindium (TMIn) provided the indium flux. Growth rates ranged from approximately 10 to 60 Å/min. InAlN layers were grown t 525°C while AlN layers were grown at 700°C. Prior to the 700°C growth, a 400°C AlN nucleation layer was grown for 5 min. GaN was grown on $LiGaO_2$ at 925°C. Surface and crystalline quality were examined by atomic force microscopy (AFM) using a DI-Nanoscope III in tapping mode, high resolution x-ray diffraction (HRXRD) utilizing a Philips 5-crystal system, and scanning electron microscopy.

The ZnO substrates were found to be highly sensitive to temperature, with even the modest temperatures needed for In-mounting (170 -190°C) resulting in a significant color change from clear to amber, easily-detectable by eye, possibly due to a change in stoichiometry. Upon heating under the nitrogen plasma in vacuum, the color change became even more pronounced. Because of this sensitivity, growth of InAlN, which can be performed at relatively low substrate temperatures, was chosen for investigation over that of InGaN which has been shown to require temperatures approximately 100°C higher to maintain the same degree of crystallinity.[48] As can be seen in Figure 3-11 both ternary systems can be lattice-matched to ZnO at the appropriate compositions. In addition to temperature, it has been previously observed for GaN on sapphire that reducing the nitrogen flow to the ECR source during growth is necessary to achieve smooth surface morphologies and good crystallinity.[33] Similar behavior was found in this study for growth of InAlN. This is not believed to be due to the effect of the nitrogen flow on the substrate surface during the initial exposure to the plasmabefore growth commences, as the flow was kept constant at 10 sccm during heat-up for all of the samples. Rather it is believed that this V/III effect is due to site-blocking by the adsorbed nitrogen at the growth surface. Using optimized conditions, the best InAlN RMS value obtained on ZnO was 3.3 nm. The lattice mismatch was measured by x-ray diffraction to be 8×10^{-3} which corresponds to an indium mole fraction of $X_{In} = 0.33$. This value was confirmed by electron microprobe analysis which indicated an X_{In} of 0.36. In spite of this relatively close lattice match, the structural quality of the material was poor as evidenced by extremely broad high resoltion x-ray peaks (much greater than 1 minute-FWHM). Furthermore, the surface morphology and crystallinity were indistinguishable from that obtained in the same growth run on severely-mismatched GaAs . Ion channeling analysis of the InAlN on ZnO shows that the crystal quality degrades severely near the substrate/film interface, suggesting that the surface of the ZnO may have degraded during heat up or that the nucleation was poor resulting in fine-grained three-dimensional growth rather than step flow. Both explanations suggest the need for a low temperature nucleation layer.

Since TMI does not decompose efficiently at low temperatures while DMEAA does, AlN buffers were the most suitable choice for use as low T buffers. In order to avoid the potential for defect generation due to the mismatch between the InAlN and the AlN buffer, AlN overlayers were grown on the low temperature AlN buffer. The use of low temperature AlN buffers does not provide substantial improvement in the material quality. Close inspection of the layer grown on ZnO shows evidence of small, somewhat random crystallites indicating a fine grained polycrystalline material. Furthermore, the crystalline quality of this film as measured by x-ray diffraction is significantly inferior to that which can be obtained on sapphire when grown under the same conditions. This difference in structural quality was also observed for the growth of AlN on (0001) sapphire and ZnO as can be seen in Figure 3-12. The poor surface morphology and broad x-ray rocking curve peaks cannot be attributed to poor ZnO substrate quality since as-received material shows a FWHM of

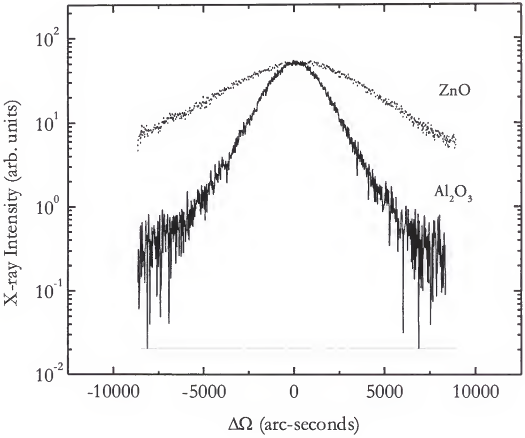

FIGURE 3-12. ΔΩ x-ray rocking curves of InAlN grown on sapphire and ZnO under identical growth conditions

only 17 arc-seconds and the surface RMS roughness as determined by AFM is routinely measured to be less than 10.0 nm. Rather it appears that the ZnO surface degrades prior to deposition, even at 400°C. This degradation may be related to the fact that ZnO is not expected to form a nitride overlayer during heat up under the plasma.

Unlike ZnO, $LiAlO_2$ and $LiGaO_2$ exhibit much higher thermal stability. As reported previously, growth of high quality GaN requires the use of relatively high (>800°C) temperatures. Fortunately, the apparent thermal stability of $LiGaO_2$ allows for such temperatures to be used. GaN growth at 925°C on (100) $LiGaO_2$ was obtained at a rate comparable to that obtained on sapphire. In spite of the reduced lattice mismatch, however, the crystal quality obtained on $LiGaO_2$ is significantly poorer than that which can be obtained on sapphire using a low temperature AlN nucleating buffer. The $\Delta\Omega$ x-ray FWHM for the $LiGaO_2$ film was approximately 7500 arc-seconds while the best results for MOMBE growth on sapphire are ~ 870 arc-seconds for similar film thickness and growth conditions. It is possible that further optimization of the nitridation of the surface may help to improve the material quality. Excellent structural quality has been reported for example in GaN grown by MOCVD on $LiGaO_2$ at slightly lower temperatures (~800°C).[49] A significant difference between these two growth techniques is the use of ammonia in MOCVD as opposed to a plasma in MOMBE. The presence of hydrogen at the growth surface from decomposed ammonia may help to form a nitride template at the surface which then allows for good quality growth without the use of a buffer layer. Clearly, further work is needed on the nucleation behavior of nitrides on these materials under UHV conditions.

In conclusion of this section, the use of oxide substrates for th growth of III-nitride materials by plasma-assisted MOMBE has been investigated. ZnO was not found to produce any improvement in material quality over what can be obtained using optimized growth conditions on (0001) sapphire. This is believed to be due to the poor thermal stability of ZnO and to the absence of the formation of a nitride layer at the substrate surface. Formation of such a layer for example, produces significant improvement in the surface morphology and structural quality of AlN and GaN grown on Al_2O_3. Preliminary experiments on $LiGaO_2$ and $LiAlO_2$ offer more promise due to the greater thermal stability, but may require the use of low temperature buffers as for sapphire to improve nucleation behavior. More research is required to understand the nucleation behavior on $LiGaO_2$ and $LiAlO_2$ before they can rival the utility of (0001) Al_2O_3 as a substrate for plasma-assisted MOMBE growth of III-nitrides.

3.3 Plasma Characteristics and the Growth of Group III-Nitrides by Metalorganic Molecular Beam Epitaxy

Improved quality and controllability of growth processes are key issues for the maturation of III-N technologies. One of the most important concerns for the growth of III-N materials in ultra high vacuum is the ability to provide an effective nitrogen source flux to the growth surface. Although the ECR plasma source was able to provide a sufficient activated nitrogen flux able to grow high quality III-N films, difficulties with contamination of the source components led to the utilization of an RF plasma source. The following experiments have sought to correlate RF plasma parameters and their impact on the growth of GaN by plasma-assisted MOMBE.

Structural quality and its relationship to point defects and mid-gap states, dopant activation, and carrier mobilities directly limit the application of III-N materials in high-efficiency, high performance devices. At present, these issues are especially relevant considering the lack of a commercially-developed homoepitaxial or lattice-matched substrate and the interest in integrating III-N:Er optical functionality with Si. Investigations of III-nitrides as hosts for 1.54 µm emitters has suggested that structural quality also plays a role in isoelectronic dopant activation.[50]

One of the greatest barriers facing the development of III-N materials has been providing an adequate Group V flux for growth at temperatures appropriate for high quality GaN and In-containing materials in MOCVD and MBE. The stability of the nitrogen molecule drives the N_2 partial pressures required for equilibrium growth of GaN to extremely high values. This has made the preparation of single-crystal GaN substrate very difficult. Certainly, it precludes the growth of GaN from thermally-decomposed N_2 in UHV. This has led researchers to develop methods to produce activated nitrogen to react with a Ga-precursor at the growth surface. These methods have included radio frequency (RF) plasma, electron cyclotron resonance plasma, and ion sources.

Substrate temperature is a critical issue for MBE growth of III-N. It presents a balance between optimized growth-mode kinetics and GaN metastability at the growth temperature. Typically, in MBE of GaAs the substrate is maintained at ~600°C, which is 58% of the melt temperature. It is thought that higher substrate temperatures enhance the surface mobilities of growth species and provide thermal energy to surmount microscopic kinetic barriers to incorporation and high quality epitaxy. However, an upper limit is placed on growth temperature by the thermally-driven volatility of the Group V species. During the growth of GaN in UHV, reactive nitrogen species must be supplied to the growth surface to drive the formation reaction. This reaction must counter the thermal decomposition of

GaN, which is metastabilized by a kinetic energy barrier at growth temperatures,[51] by the following equation:

$$\mathrm{GaN(s)} \quad \rightarrow_{\Delta G = -1.8\ \mathrm{eV}} \quad \mathrm{Ga(l)} + \tfrac{1}{2}\,\mathrm{N_2(g)} \qquad \{800^{\circ}\mathrm{C},\ 10^{-6}\ \mathrm{Torr}\}$$

However, higher substrate temperatures, as in conventional III-V MBE, generally lead to improved III-N epitaxy. Generally, MOCVD of high-quality nitride films is conducted at temperatures near 1000°C.[40,52] It was shown in the first section of this chapter that higher substrate temperatures (>900°C) favor higher structural quality and lower mid-gap optical absorption in plasma-assisted MOMBE of GaN.[33] Investigations of MBE GaN growth from ECR plasmas has shown a detrimental correlation between increased microwave power and growth quality.[53] This deterioration in structural quality was attributed to the negative impact of high energy ionic nitrogen species. However, such pronounced effects were not observed for high quality ECR-derived material deposited under different forward powers at higher growth rates (~0.5 μm/hr) during the MOMBE experimentation previously outlined.[33] Hughes et al.,[54] have compared the growth of GaN by MBE using ECR and RF sources and introduced the idea of utilizing optical emission spectroscopy (OES) as a plasma diagnostic tool for plasma-assisted MBE growth of nitride film. Their experiments attributed the higher quality material grown with the RF source to the larger amount of molecular and atomic neutral nitrogen present in the RF discharge, indicated by optical emission spectra, as compared to that seen in the ECR plasma under similar conditions. However, growth of high quality material from ion sources has also been demonstrated.[55,56] The research outlined here has sought to correlate growth experiments and selfconsistent optical emission spectral analysis of RF plasmas to better understand the role of atomic nitrogen and optimize plasma-assisted MOMBE of GaN.

The following growth experiments were conducted with the SVT Associates RF plasma source configured as presented in Chapter 2. All tuning of the plasma was done manually. Optical emission spectra were taken with a Verity Inc. VM2000 monochromator-based optical emission spectrometry system. Light from the plasma was collected into a fiber bundle from a rear window directly integrated into the back of the RF plasma source. This light was then directed into a grating monochromator and the resulting signal was detected using a photomultiplier tube. The RF nitrogen plasma optical emission spectra observed with this OES setup shows dominant lines near 740 nm, 820 nm, and 860 nm associated with the 3s ^4P- 3p $^4S^\circ$, 3s ^4P-3p $^4P^\circ$, and 3s ^2P- 3p $^2P^\circ$ and 3s ^4P- 3p $^4D^\circ$ multiplets, respectively, indicating the presence of significant amounts of atomic nitrogen. Figure 3-13 depicts a portion of the RF nitrogen spectra collected from a plasma sustained at 400 W of forward RF power and 4 sccm of N_2. All spectra collected for the range of RF conditions in this work were of this form. The profile of this spectra contrasts with that of an ECR nitrogen plasma operating at 5 sccm and 200 W forward power, shown in Figure 3-14. In the ECR spectrum atomic nitrogen emission is less pronounced relative to the intensity of emission from ionic species. This is in agreement with RF and ECR optical spectra observed independently.[53]

Plasma optical emission spectra were collected and analyzed for a range of plasma conditions. Figure 3-15 presents atomic nitrogen OE line intensity as a function of N_2 flow rate for three different forward powers: 300W, 400W, and 500W. For a given RF power, the intensity of the atomic nitrogen-related optical emission goes through a maximum. This

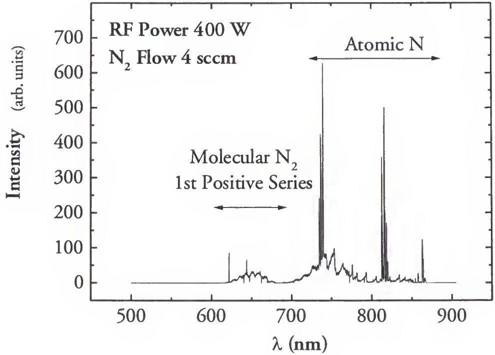

FIGURE 3-13. Optical emission spectrum of an RF nitrogen plasma discharge collected from the rear window of the SVT Associates RF source.

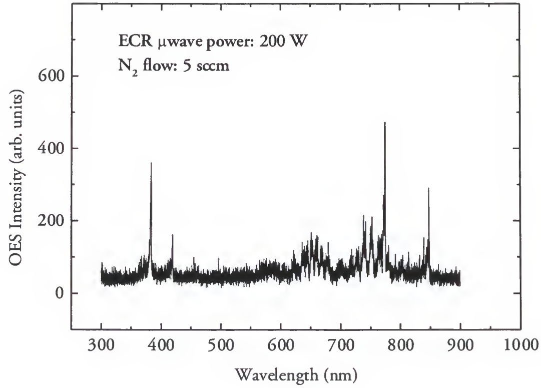

FIGURE 3-14. Optical emission spectrum of an ECR nitrogen plasma discharge collected through a source-facing growth chamber window.

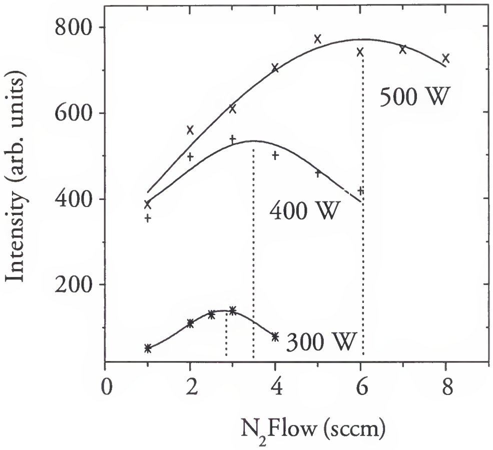

FIGURE 3-15. Atomic nitrogen optical emission intensity as a function of N_2 flow into the plasma chamber for three different RF forward powers

behavior can be explained by a two regime model depicted in Figure 3-16. Below the atomic nitrogenintensity maximum, sufficient RF energy is available to dissociate the N_2 present in the plasma chamber. The abundance of monatomic nitrogen is limited by the pressure and, therefore, the flow rate of N_2 into the plasma chamber. At higher flow rates, the plasma chamber pressure increases and the RF energy available per ion decreases. Above the intensity maximum, the energy per N_2 molecule is no longer sufficient to dissociate all the available nitrogen. The endpoints of each curve are defined by the minimum or maximum flow rate at which a plasma can be maintained and the maximum power that can be coupled into the source with our experimental apparatus. There is also the possibility that at higher flow rates and higher plasma densities in the chamber, another activated nitrogen complex becomes dominant. However, within the range of the spectrometer system, no other emission lines that followed such behavior were found. All lines in the collected spectra, including those of ionic species, followed the same general behavior of the atomic nitrogen lines.

The effect of increasing power on atomic nitrogen intensity is shown in Figure 3-17. Generally, as power increases for a given nitrogen flow rate the atomic N intensity increases monotonically. For a limited range of atomic nitrogen intensities, there are two sets of flow and power conditions that could create that intensity. For example, a nitrogen plasma operating at 400 W forward RF power and 3 sccm N_2 flow produces an atomic nitrogen intensity roughly equivalent to that observed for a plasma maintained at 500 W RF forward power and 2 sccm N_2. However, the growth rate of GaN at a substrate temperature of 925 °C and a constant Group III flux observed for these two plasma conditions were markedly different as can be seen in Figure 3-18. Growth with 400 W RF forward power and 3 sccm

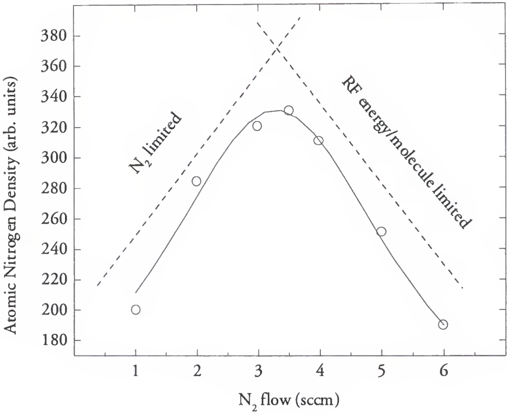

FIGURE 3-16. Two regime model for the atomic nitrogen density as a function of flow rate for a fixed RF power. At lower flows, the atomic nitrogen density is limited by the availibility of N_2. At higher flows the amount of energy available per molecule is not enough to dissociate N_2, limiting the N abundance.

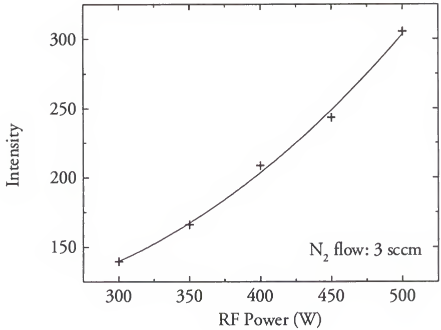

FIGURE 3-17. Atomic nitrogen OES intensity as a function of RF power with the supply of N_2 to the plasma chamber held constant.

of N_2 flow proceeded at a rate of ~5100 Å/hr. However, the growth rate dropped to ~1200 Å /hr utilizing an RF forward power of 500 W and a N_2 flow of 2 sccm. This disparity in growth rate under conditions that produce the same atomic nitrogen OES intensity suggests that other species or effects must strongly influence growth. For these two conditions, the energy coupled into the plasma per nitrogen molecule nearly doubles. The growth rate returned to ~5000 Å when the N_2 flow rate was increased to 5 sccm with 500 W of RF power. However, the morphology of growth under these high atomic nitrogen plasma conditions was poor. This parallels results observed in ECR-derived material in which higher N_2 flow led to poorer structural quality.[10] Figure 3-19 shows the GaN growth rate as a function of (RF power)/(N_2 flow) with units of [W/sccm]. At high growth temperatures,

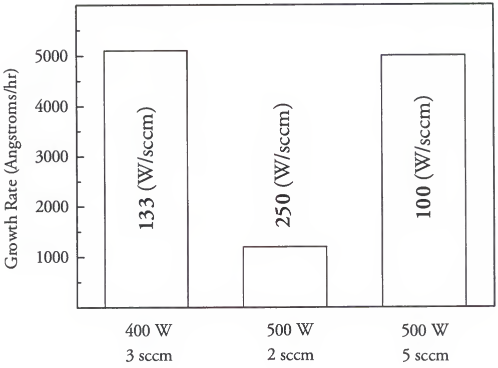

FIGURE 3-18. Gallium nitride growth rates under different plasma RF powers and N_2 flow rates. The y-axis labels denote the plasma power and flow conditions used to produce the specified growth rate. The corresponding power/flow ratio is indicated vertically for each case.

GaN UHV growth occurs when the arrival rate of effective activated species overcomes the dissociation rate. The increase in the power/flow ratio can affect this reaction in a number of ways either decreasing the flux of effective activated species, increasing the dissociation rate, or promoting sputtering.

If the decrease in growth rate is due to a reduction in the effective activated species flux, this suggests that atomic nitrogen is not the only growth species responsible for GaN growth from an RF plasma. Either the increased power/flux results in a decrease in the other reac-

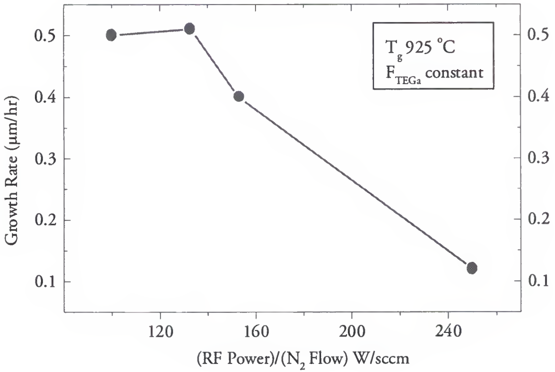

FIGURE 3-19. Gallium nitride growth rates as a function of plasma RF power/nitrogen flow ratio.

tive species responsible for growth such as N_2^* or N_2^+, or the increase in energy per molecule result in a reduced surface lifetime for the reactive nitrogen species and a lowered effectiveness for driving the metastable growth reaction. It is also possible that the increase in energy per molecule directly effects the dissociation rate. This possibility may be particularly relevant for growth at high temperatures (greater than 900 °C) where the growth rate would by critically affected by the dissociation rate.[53,57] In this case high energy species at the growth front could drive the dissociation process. RF plasma exposure experiments were conducted during which previously deposited GaN films maintained at 925 °C were subjected to 400

W/ 3 sccm N_2 and 500 W/2 sccm N_2 plasmas. Preliminary results indicate that a higher (RF power)/(N_2 flow) ratio favors GaN dissociation and possibly preferential nitrogen loss resulting in etching and a marked increase in n-type conductivity.

In conclusion, optical emission spectroscopy has been used to optimize atomic nitrogen production from an RF plasma source. Growth of GaN under equivalent amounts of atomic nitrogen, as determined by OES, but different (power)/(N_2 flux) ratios indicated that the presence of atomic nitrogen alone is not a sufficient condition for growth. Reductions in the abundance of other activated species or the enhancement of the dissociation rate due to increased kinetic energy of species impinging on the growth surface lead to reduced growth rates (from 0.5 μm/hr to 0.12 μm/hr). Under very high atomic nitrogen flux and low energy per molecule plasma conditions the growth rate saturates but film quality degrades in a manner similar to that observed for ECR-derived GaN grown under high flow conditions.

CHAPTER 4
ALUMINUM NITRIDE DOPED WITH ERBIUM DURING GROWTH BY PLASMA-ASSISTED METALORGANIC MOLECULAR BEAM EPITAXY

The potential for 1.54 µm semiconductor electronics was discussed in Chapter 1. In this portion of the dissertation research, AlN has been doped with Er during growth by plasma-assisted metalorganic molecular beam epitaxy (MOMBE) using metalorganic and elemental sources. This work was undertaken to demonstrate, for the first time, optically active Er^{3+} in a III-N semiconductor doped during growth and to evaluate the incorporation behavior of Er from metalorganic and solid sources. AlN was chosen as the first matrix material for Er due to its wide band gap (6.2 eV) and high ionicity. Trends observed for Er incorporation in other semiconductor materials have indicated a significant increase in laser-induced photoluminescence (PL) with increasing band gap.[9] Concurrent with this trend, it has also been suggested that the electronic environment provided by more ionic semiconductor hosts enhances the intra 4f shell Er^{3+} transitions responsible for the desired optical emission.[5] Upon co-implantation of Er and O, Fl and other species into Si substantial increases in 1.54 µm PL have been reported.[11,58] It has been theorized that the presence of ionic species alter the local field environment of the Er^{3+} ions enhancing the optical activity. Based on this evidence,, wide band-gap, ionic compound semiconductors including II-VI materials and the III-nitrides are promising hosts for rare-earth dopants. The structural and thermal stability of AlN and GaN make them particularly attractive for reliable, long service-life applications.

Luminescence from Er implanted into the III-nitrides was first observed by Wilson et al.[59] Photoluminescence at 1.54 μm attributed to transitions between Er^{3+} $^4I_{13/2}$ and $^4I_{15/2}$ levels was observed in ion-implanted GaN and AlN. However, Er^{3+} luminescence from the AlN was seen only at low temperatures. Developing on this work, solid source- and metalorganic- Er doping of AlN during growth by plasma-assisted metalorganic molecular beam epitaxy has been demonstrated. Doping during growth has several advantages over ion implantation. It can be a more flexible technique than ion implantation for many growth applications due to the absence of ion damage, unlimited layer thickness, and better doping profile control.

The AlN films discussed in this study were grown by plasma-assisted MOMBE in an INTEVAC Gas Source Gen II on In-mounted (0001) Al_2O_3 and (001) semi-insulating GaAs as described in Chapter 2. All films were preceded by a low temperature AlN buffer (T_g 425 °C). Dimethylethylamine alane (DMEAA) maintained at a bubbler outlet pressure of 7.6 Torr and a bath temperature of 9.3 °C provided the Group III fluxes. The DMEAA was transported to the gowth chamber with a He carrier gas flow of 10 sccm. Reactive nitrogen for the growth of AlN was provided by a Wavemat MPDR 610 electron cyclotron resonance (ECR) plasma source with an Al_2O_3 plasma chamber. A shuttered effusion oven charged with 4N Er was used for solid-source doping. Erbium-doped layers were preceded by 2000 Å of undoped AlN. Erbium incorporation was profiled by secondary ion mass spectrometry (SIMS). Al, N, and O levels were also monitored during the SIMS profiling. Room and low temperature photoluminescence was used to evaluate the Er^{3+} optical activity.

For the AlN:Er thermal-quenching measurements the AlN:Er^{3+} PL was excited using the 488 nm line of an Ar ion laser and measured with a liquid nitrogen-cooled Ge detector. A He refrigerator capable of reaching temperatures as low as 12K was used to cool the sample. Surface composition was analyzed with a scannnig Perkin-Elmer Auger electron spectroscopy (AES) apparatus.

Erbium concentrations from 3×10^{17} cm^{-3} to 2×10^{21} cm^{-3}, as determined by SIMS, were achieved for effusion cell temperatures ranging from 955 °C to 1343 °C. This dynamic range is represented in Figure 4-1 where an Arrhenius-like thermal activation energy

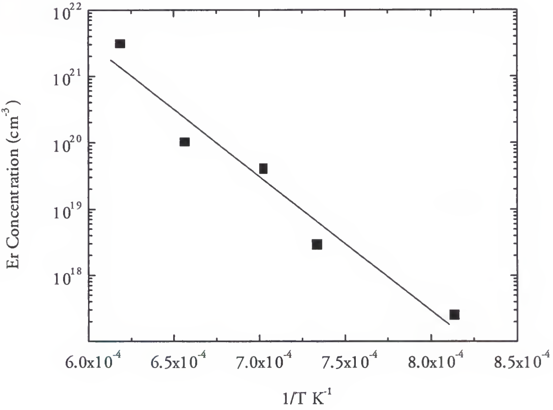

FIGURE 4-1. Erbium concentration as a function of the inverse of the effusion cell temperature

of approximately 4.0 eV was fit to the observed Er incorporation behavior. This is comparable to the corresponding ~3.0 eV activation energy for the vapor pressure of Er in this temperature range.[61] Strong 1.54 μm Er^{3+} photoluminescence was observed in AlN:Er doped to concentrations greater than 3 x 0^{18} cm^{-3}. The 5K PL intensities (pump wavelength = 458 nm) excited these films were nearly two orders of magnitude greater than those observed in AlN implanted with Er to similar levels as can be seen in Figure 4-2. AlN:Er films deposited on GaAs showed considerably weaker PL at low temperatures than AlN:Er

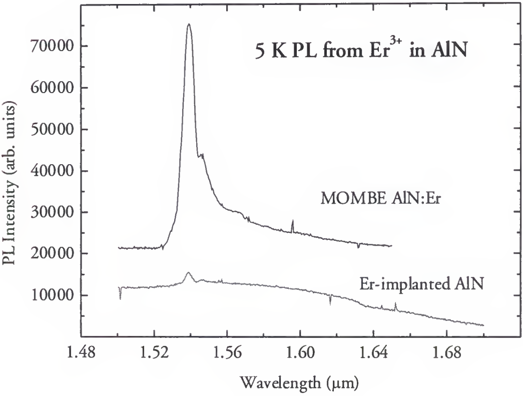

FIGURE 4-2. Comparison of 5K PL from MOMBE-derived AlN:Er and Er-implanted AlN ([Er] ~ 10^{19} cm^{-3}).

grown on Al_2O_3 while no 1.54 μm signal was detected at room temperature for AlN:Er/GaAs. High resolution x-ray diffraction rocking curves for the AlN:Er on GaAs were very diffuse indicating poor epitaxial crystallinity. Considerably stronger Ω-scan X-ray peaks with half-widths of 6100" and 6800" were observed for AlN grown on (0001) sapphire with Er concentrations of 3×10^{17} cm^{-3} and 2×10^{21} cm^{-3}, respectively. This indicates that AlN structural quality has a significant effect on the optical activity of Er^{3+} as room temperature PL was not observed for AlN:Er on GaAs. As well, increasing the erbium concentration adversely affects the epitaxial crystallinity of the AlN matrix.

Oxygen backgrounds of ~2×10^{20} cm^{-3} were observed in all AlN samples. Sputtering of oxygen from the alumina ECR plasma cup is believed to be one of the sources of this oxygen. Thermal-quenching experiments indicated that 488 nm-pumped Er^{3+}-related PL quenches by approximately a factor of two between 15K and 300K for AlN:Er doped 2-5 x 10^{19} cm^{-3}. The temperature dependence of the Er^{3+} luminescence is shown in Figure 4-3. This quenching behavior for MOMBE-derived AlN:Er compares favorably with that of other semiconductor hosts as can be seen in Figure 4-3.[5,9,60] Dramatically less quenching was observed for solid source-doped AlN:Er than has been reported for Si or GaAs.

Rounded surface features, observed on AlN:Er by SEM, increased in size from approximately 1-2 μm (T_{cell} 955°C) to ~3-5 μm (T_{cell} 1343°C). Figure 4-4 compares the surfaces of undoped AlN, AlN:Er (3 x 10^{17} cm^{-3}, and AlN:Er (2 x 10^{21} cm^{-3}). Auger electron spectroscopy analysis indicates that the surface features present in these SEM micrographs are not Er droplets. This is also supported by the absence of an [Er] surface spike during dynamic SIMS profiling.

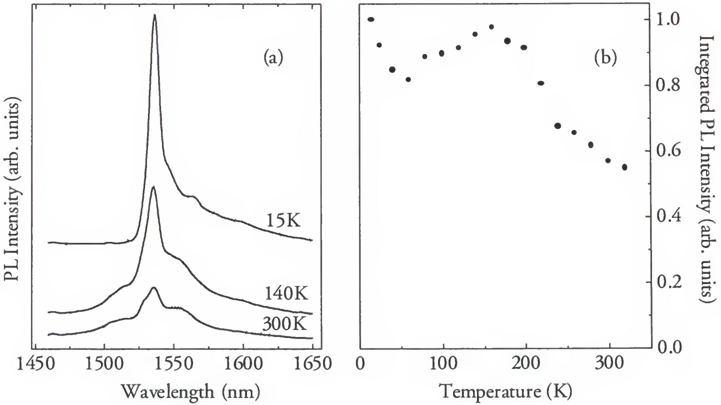

FIGURE 4-3. Temperaure dependence of AlN:Er PL spectra (right) and Er^{3+} integrated photoluminescence intensity (left) on temperature.

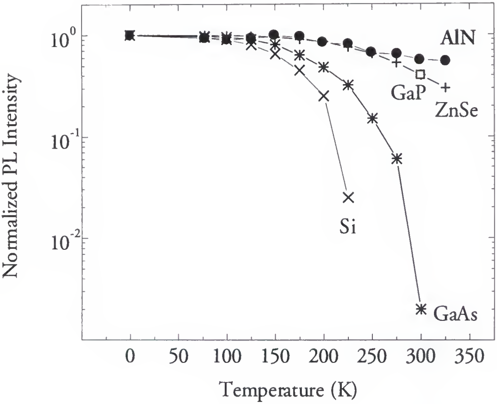

FIGURE 4-4. Comparison of 5K PL from MOMBE-derived AlN:Er and Er-implanted AlN ([Er] ~ 10^{19} cm^{-3}).[5,9]

The effect of growth temperature on the sticking coefficient of Er was also investigated with a specialized growth sequence and SIMS. A film stack consisting of three layers of AlN:Er, each ~1000 Å, grown at 800°C, 600°C, and 500°C, and separated by 500 Å of undoped AlN was deposited on Al_2O_3 following a low temperature buffer layer. The stack was capped with ~1000 Å of undoped AlN. A constant Er cell temperature of 1090°C was maintained during the growth of all three layers. The dynamic SIMS profile of this sample is shown in Figure 4-5. This profile indicates that the Er concentration fell by nearly a factor

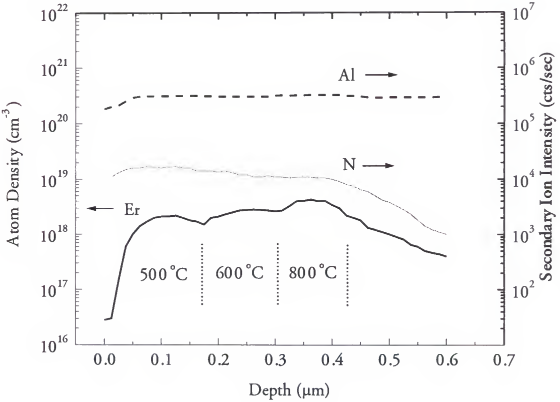

FIGURE 4-5. Comparison of 5K PL from MOMBE-derived AlN:Er and Er-implanted AlN ([Er] ~ 10^{19} cm^{-3}).

of two as the growth temperature was reduced from 800°C to 500°C . This behavior suggests that solubility effects may limit the Er incorporation efficiency. The absence of Erbium accumulation at the surface or other profile features indicates that solid-source Er does not segregate strongly during growth.

AlN was doped with Er using metalorganic precursors, including Erbium tris (2,2,6,6-tetramethyl-3-5-heptanedionate) {Er(TMHD)$_3$} and Erbium tris (bis trimethylsilylamide) {Er(BTSA)$_3$}. The molecular structures of Er(TMHD)$_3$ and Er(BTSA)$_3$are represented in Figure 4-6. The oxygen and nitrogen bonded to the Er in these precursors were hoped to have interesting implications for Er incorporation and activation in AlN. Erbium 1.54 µm PL was observed for AlN:Er doped during growth with fluxes of Er(TMHD)$_3$ and Er(BTSA)$_3$. Figure 4-7 shows room temperature PL from AlN:Er doped with Er(TMHD)$_3$ to an Er concentration of approximately 10^{17} cm^{-3}. The intensity of this 1.54 µm-region PL is several orders of magnitude less than that observed for solid source-doped AlN:Er. In order to

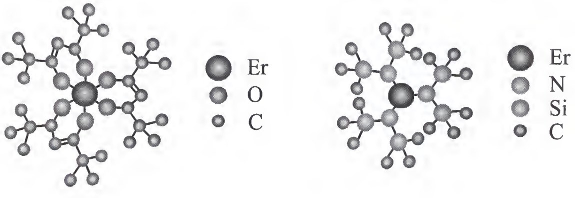

FIGURE 4-5. Erbium tris (2,2,6,6-tetramethyl-3-5-heptanedionate) {left} and Erbium tris (bis trimethylsilylamide) {right} molecular structures.

produce this 10^{17} cm^{-3} doping level, the metalorganic source bubblers were mounted directly to the injectors on the source flange and the bubbler and delivery lines were heated to 100 °C. As this temperature represents an upper practical limit for source module operation, it appears that higher vapor pressure metalorganic sources are required.

In summary, AlN:Er films exhibiting room temperature PL have been grown by MOMBE. Low temperature PL intensity was more than two orders of magnitude higher in AlN:Er/Al_2O_3 films than in implanted AlN. Low temperature 1.54 μm PL was less intense

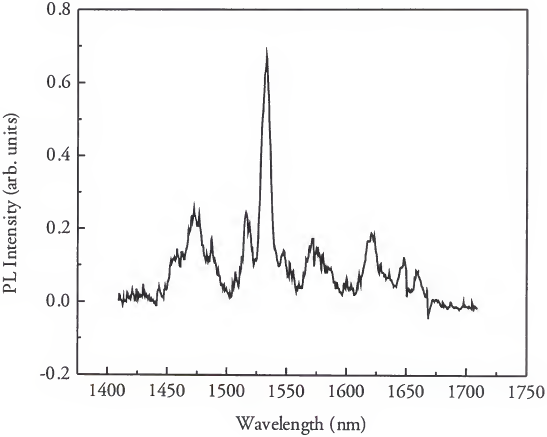

FIGURE 4-6. Room temperature PL from AlN:Er doped using the Er TMHD metalorganic precursor. [Er] was approximately 10^{17} cm^{-3}.

for AlN:Er samples grown on GaAs than for those grown on Al_2O_3 indicating that structural quality has a considerable effect on Er optical activity. Erbium appears to impact structural quality as indicated by a coarsening in surface features and a degradation in epitaxial crystallinity with increasing Er concentration. A slight reduction in incorporation efficiency was observed at lower growth temperatures. Thermal quenching experiments showed a reduction of nearly 50% in 1.54 μm PL signal from AlN:Er between 15K and 300K demonstrating a substantially higher temperature limit than conventional III-V materials[9,61] and Si.[9] Two metalorganic precursors, $Er(TMHD)_3$ and $Er(BTSA)_3$, were utilized to dope AlN with Er during growth. However, the low vapor pressure of these sources limited doping levels and PL intensities considerably below that possible with solid-source doping. The results observed in this chapter firmly demonstrated the potential for Er luminescent centers in Group III nitrides grown by MOMBE as a technologically-significant near-IR material.

CHAPTER 5

GROWTH AND LUMINESCENCE PROPERTIES OF GALLIUM NITRIDE DOPED WITH ERBIUM DURING GROWTH BY PLASMA-ASSISTED METALORGANIC MOLECULAR BEAM EPITAXY

The scope of this chapter includes an investigation of the incorporation and optical activation of Er introduced into GaN during growth by plasma-assisted metalorganic molecular beam epitaxy (MOMBE). Radiative intra-4f shell transitions in Er at 1.54 µm match the attenuation loss minima in silica fibers.[1] The possibility of creating efficient, temperature-stable 1.54 µm emitters for fiber communications systems has stimulated interest in rare earth-doped semiconductor optoelectronics. Considerable research work has been devoted to studying the incorporation and optical activity of Er in Si[62-65] and III-V materials.[60,66-69] The initial drive for 1.54 µm emission from Er^{3+} in Si sought to overcome the intrinsic, indirect band-gap. Such a development, in its mature form, would establish the basis of an integrated Si optoelectronic technology with immense commercial potential. This Si:Er research uncovered two significant aspects of Er optical activation. The luminescence efficiency of Si:Er decreases dramatically with increasing temperature such that the Er^{3+} luminescence at room temperature was only a small fraction of the low temperature emission. Also, the symmetry and local electronic environment of the Er dramatically impacts the luminescence efficiency. Influencing the local environment with the introduction of electronegative species such as O, N, and F resulted in significant increases in Er^{3+}-related emission. Favennec et al.[9] demonstrated a reduction in thermal quenching with increasing bandgap for a range of Group IV, III-V, and II-VI semiconductors doped by ion-implantation. It has also been suggested that the ionic nature of a particular host matrix can enhance the radiative efficiency of Er^{3+}. Neuhalfen and Wessels[61] confirmed this trend in $In_xGa_{1-x}P$.[60] In the previous chapter, room temperature PL from Er-doped AlN was investigated. Although the 6.2 eV band gap of AlN is an attractive attribute for an Er host, the possibilities for exploiting AlN:Er in optoelectronic structures is limited. There has been little success in electrically doping AlN. And, the wide energy gap leads to very large band offsets, and thus barriers to carrier injection at heterojunctions. On the other hand, GaN, with a band gap of 3.4 eV, can be doped n- and p-type and has been incorporated in heterostructure light-emitting diodes and field-effect transistors.

Ion implantation has been utilized by a number of research groups to demonstrate Er^{3+}-related 1.54 μm luminescence in GaN.[70-73] However, the large Er mass and the high energies required to implant Er restrict the depth and distribution of the Er profile. Also, at higher doses the implantation process can cause significant damage in the host matrix. This can be particularly troublesome in III-N materials which have a limited ability to recover damage through annealing. In this work, solid-source doping during MOMBE growth has been employed to achieve optically active Er in GaN grown on Al_2O_3 and Si.

All GaN:Er films in this study were grown by MOMBE in an INTEVAC Gas Source Gen II on In-mounted (0001) Al_2O_3 and (111) Si. GaN films were preceded by a low temperature AlN buffer (T_g ~ 425°C). A 0.2 μm undoped GaN spacer was deposited prior to the growth of GaN:Er as depicted in Figure 5-1. Dimethylethylamine alane (DMEAA), triethylgallium (TEGa), and thermally-evaporated 8N Ga metal provided the Group III fluxes. A shuttered effusion oven charged with 4N Er produced the dopant flux. Reactive nitrogen species were provided by an SVT RF plasma source fed with megabit purity N_2. Further details of thegrowth procedures are outlined in Chapter 2.

Erbium incorporation was profiled by dynamic secondary ion mass spectrometry (SIMS). Ga+N, O, and C levels were also monitored. Erbium PL was excited using the 488 nm line of an Ar ion laser and measured with a Ge detector. A He refrigerator capable of reaching temperatures as low as 12K was used during the thermal quenching measurements. Scanning electron microscopy and x-ray diffraction were used to evaluate structural quality.

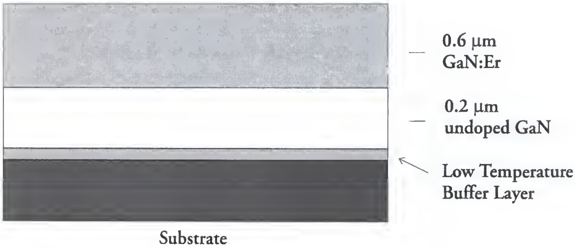

FIGURE 5-1. 1.54 μm-region, room temperature PL spectra from TEGa-derived GaN:Er grown on Al_2O_3 and Si.

Room temperature PL was observed for GaN:Er films grown on (0001) Al_2O_3 and (001) Si. Photoluminescence spectra of the 1.54 µm region, measured at 300K from TEGa-derived GaN doped during growth to an Er concentration of approximately 3×10^{18} cm^{-3} on Al_2O_3 and Si are shown in Figure 5-2. The intensity of the PL from these samples was several orders of magnitude brighter than for AlN:Er doped during growth on Al_2O_3. The peak widths and absence of fine structure in the Er^{3+} emission observed in these samples may be due to the high density of active Er states and a continuum of varying local field environments due to the proximity of impurities, native defects, other Er atoms or structural de-

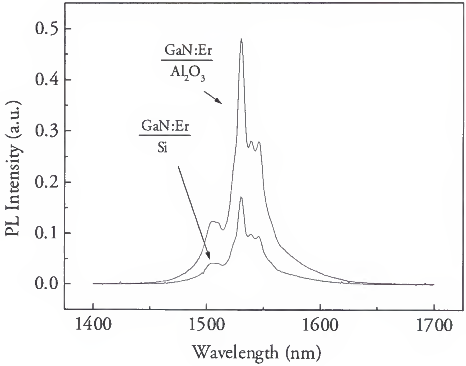

FIGURE 5-2. 1.54 µm-region, room temperature PL spectra from TEGa-derived GaN:Er grown on Al_2O_3 and Si.

fects within the GaN. The spectral shape near 1.54 μm for the highly luminescent GaN:Er resembles the spectra of erbium-doped silica fibers which have high concentrations of optically-active Er.[1] Rutherford backscattering studies of Er-implanted GaN grown by MOCVD indicate that the erbium, before and after annealing, resides predominantly in substitutional lattice positions.[74] Figure 5-3 shows the Er and Ga backscatter yields for an implanted and annealed sample as a function of angle around the <0001> and <10-11> channeling directions. The Er yield minima closely follows that for Ga indicating the absence of Er in the interstices. Thermal annealing had little noticeable affect on these angular backscatter profiles suggesting that the implanted erbium had reached its equilibrium location. As plasma-assisted MOMBE growth is a controlled metastable process, it is expected that Er incorporated into GaN during MOMBE growth would be even more likely to reside on equilibrium sites. This suggests that erbium in MOMBE-derived GaN is likely to be substitutional. Figure 5-4 show the photoluminescence excitation spectrum of the $^4I_{13/2}$ - $^4I_{15/2}$ 1.54 μm Er^{3+} transition in MOMBE-derived GaN:Er grown on Si. Optical pumping is clearly enhanced at energies directly attributable totransitions involving higher energy 4f Er^{3+} states. Though the polycrystalline GaN inherently has a high level of planar defects, no broadband, defect-state pumping, such as that seen in the photoluminescence excitation of Er-implanted GaN,[74] was observed.

X-ray diffraction and SEM analysis indicated that the GaN:Er deposited on Al_2O_3 is columnar epitaxial with $(0001)_{GaN}||(0001)_{Al2O3}$. Highly polycrystalline GaN:Er films grown on (001) Si also exhibited strong room-temperature Er^{3+} PL. Scanning electron microscopy indicates that GaN:Er grown on Si posseses a grain size of ~0.2 μm. This polycrystallinity is likely due to structural mismatch between GaN and Si and the possibly the formation of

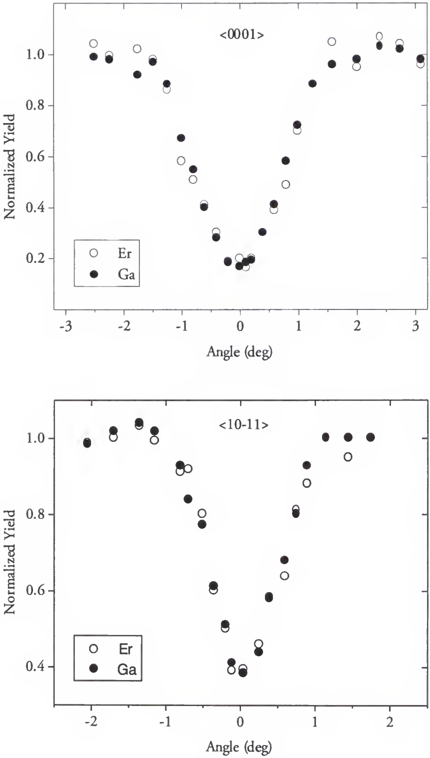

Figure 5-3. Rutherford backscatter ion channeling yield as a function of beam angle to the <0001> and <10-11> directions in Er-implanted GaN (160 keV, dose: 5 x 10^{14} cm^{-2}) after annealing at 600 °C for 30 min.

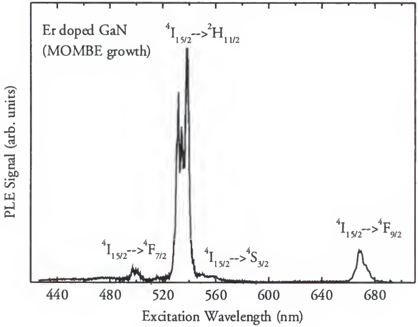

FIGURE 5-4. Photoluminescecne excitation spectroscopy of MOMBE-derived GaN:Er/Si showing the optical pumping pumping of the $^4I_{13/2}$ - $^4I_{15/2}$ 1.54 µm Er^{3+} transition from states atributed to higher energy 4f Er^{3+} levels (see Figure 1-2).

a SiN_x interfacial layer during the heat-up and plasma exposure period prior to growth. As can be seen in Figure 5-5, the integrated 1.54 µm signal from TEGa-derived GaN:Er deposited on Si is 35% of that measured for films grown under identical conditions on (0001) Al_2O_3. Figure 5-4 shows the thermal quenching behavior of the integrated Er^{3+} PL signal for TEGa-derived GaN:Er samples deposited on Al_2O_3 and Si. The 1.54 µm luminescence from the GaN:Er deposited on Si quenched by 40% between 15 K and 300 K. The more intense Er^{3+} PL signal observed for the GaN:Er grown on Al_2O_3 quenched by only approximately10% over the same temperature range with an intermediate maximum near 240 K.

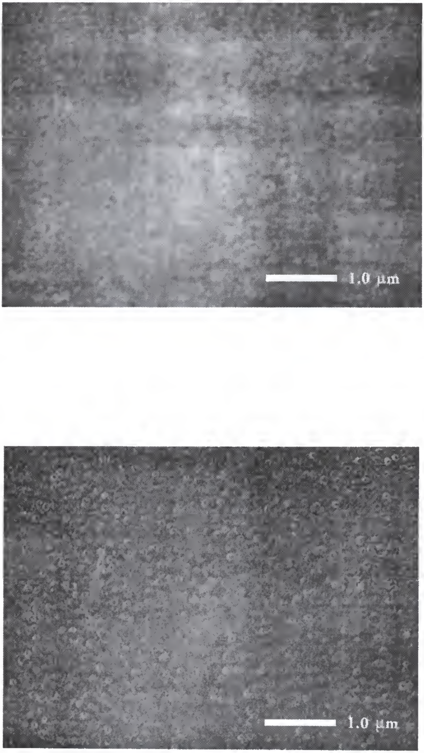

FIGURE 5-5. Scanning electron micrographs of GaN:Er grown on sapphire (top) and silicon (bottom).

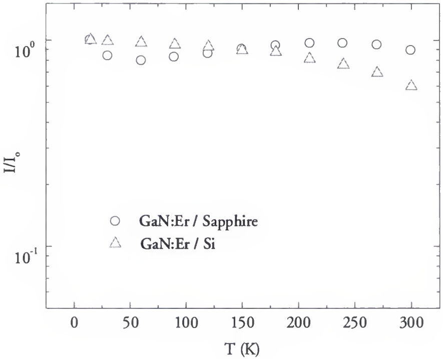

FIGURE 5-6. Temperature dependence of 1.54 μm Er^{3+} PL of TEGa-derived GaN:Er grown on Al_2O_3 and Si.

This quenching behavior may be due to the thermal activation of defect states such as those associated with carbon and oxygen that assist in energy transfer to Er^{3+}. The presence of surface defects in the polycrystalline GaN:Er on Si may compensate these states inhibiting luminescence enhancement through this excitation pathway. However, the room-temperature PL signal for TEGa-derived GaN:Er on Si is still quite significant, indicating the possibility for integrating GaN:Er and Si device technologies .

Growth experiments demonstrated that carbon and oxygen backgrounds dramatically influenced the optical activation of Er in GaN. This is shown in Figure 5-7 for two GaN

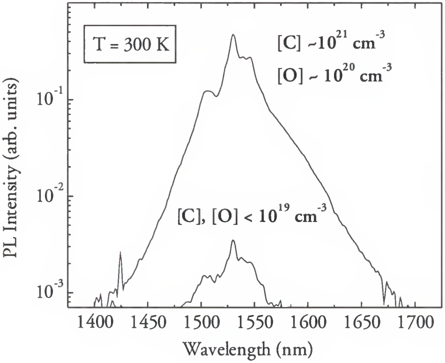

FIGURE 5-7. 300K PL spectra from GaN:Er derived from TEGa (high [C] and [O]) and 8N Ga (low [C] and [O]).

samples doped with erbium to a concentration of ~3 x 10^{18} cm^{-3} but with differing carbon and oxygen backgrounds. Due to incorporation of carbon and oxygen from residual ether in the TEGa and Ga alkoxides, the C and O backgrounds observed in TEGa-derived GaN were ~10^{21} cm^{-3} and ~10^{20} cm^{-3}, respectively, as determined by SIMS. GaN grown using thermally-evaporated 8N pure Ga as the Group III source had C and O backgrounds of less than 10^{19} cm^{-3}. The 1.54 μm Er^{3+} PL signal from TEGa-derived GaN:Er with high C and O concentrations was nearly two orders of magnitude higher than that from GaN:Er with [C] and [O] < 10^{19} cm^{-3}. The presence of high levels of carbon and oxygen also influenced

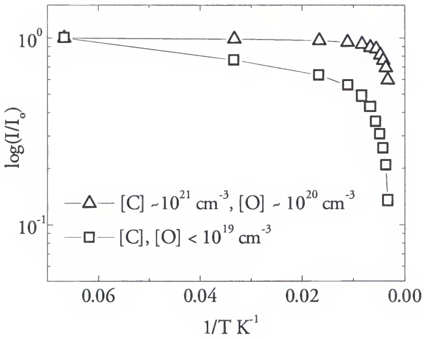

FIGURE 5-8. 300K PL spectra from GaN:Er derived from TEGa (high [C] and [O]) and 8N Ga (low [C] and [O]).

the thermal quenching behavior of the 1.54 μm PL from GaN:Er on Si and Al_2O_3. Photoluminescence signal from the sample grown with TEGa quenched by 40% between 15 K and 300 K while lower [C] and [O] GaN:Er derived from elemental Ga quenched by 85%. For GaN:Er on Al_2O_3, the differences in thermal behavior were even greater. While signal from the low [C] and [O] GaN:Er / Al_2O_3 quenched by ~85%, the high [C] and [O], TEGa-derived material grown on Al_2O_3 quenched by only ~10%. These improvements in optical activation of Er in the presence of significant concentrations of carbon and oxygen parallel the effects observed previously for light elements in Er-implanted GaN and Si. Temperature-dependent Hall-effect measurements were peformed on the GaN:Er/Al_2O_3

sample at temperatures from 5K to room temperature. No measureable conductivity was detected in this range. Further experimentation to resolve the effects of carbon and oxygen on GaN:Er optical activity is presented in Chapter 6.

In conclusion of this chapter, strong room-temperature 1.54 μm photoluminescence has been observed for GaN doped with Er during growth by MOMBE on Al_2O_3 and Si substrates. While the poorer structural quality of GaN:Er grown on (001) Si had a somewhat detrimental effect on 1.54 μm luminescence, the Er^{3+} PL from GaN:Er / Si was still considerable, suggesting the possibility for the integration of GaN:Er and Si for optoelectronic applications. Higher levels of carbon and oxygen were shown to dramatically increase the optical activity and decrease the thermal quenching of Er in GaN grown on either substrate. These results demonstrtate the potential for GaN:Er as a near-IR optoelectronic device materials with the possibility of direct integration with silicon.

CHAPTER 6

OPTICAL AND ELECTRICAL EXCITATION OF METALORGANIC MOLECULAR BEAM EPITAXY-DERIVED GaN:Er STRUCTURES INTEGRATED WITH SILICON

In this chapter, the optical and electrical excitation of Er^{3+} in GaN device structures on Si are discussed. Room-temperature electroluminescence (EL) from simple metal/GaN:Er/Si structures has been demonstrated. Also, Er excitation models in other semiconductor:Er systems are discussed and compared to the GaN:Er results observed in this work. Luminescence, implantation and annealing experiments to further elucidate the optical excitation mechanisms in MO-MBE-derived GaN:Er are presented.

Electroluminescent structures were fabricated from TEGa-derived GaN:Er films grown on p-type (001) Si. The film stack consisted of approximately 6000 Å of GaN solid source-doped with Er to a concentration of $\sim 3 \times 10^{18}$ cm^{-3}, a 2000 Å GaN spacer layer, and a low temperature AlN buffer as in Figure 5-1. Secondary ion mass spectrometry (SIMS) analysis indicated that the GaN films had carbon and oxygen concentrations of $\sim 10^{21}$ cm^{-3} and $\sim 10^{20}$ cm^{-3}, respectively. Metallized contacts were made to front and backside with the assistance of Dr. Fan Ren at Lucent Technologies in Murray Hill, New Jersey (now in the Department of Chemical Engineering, University of Florida). A cross-section diagram of the metal-GaN:Er-Si structure is shown in Figure 6-1. A scanning electron micrograph of the topside of the structures showing the patterned top-contact metallization is shown in Figure 6-2. Room-temperature electroluminescence was observed in this structure under high, reverse-bias (>20 V) conditions, demonstrating for the first time, near-infrared electroluminescence from GaN:Er grown directly on a Si substrate. A preliminary 1.54 μm-region EL spectra is shown in Figure 6-3. The energy transfer mechanism causing this emission is most likely impact excitation of Er or Er-complexes by electrons accelerated in the applied field. An estimation of the average transfer of energy from the applied electric field to the electron kinetic energy, assuming isotropic scattering, is given by: $(qE_{el}\lambda)^2/4E_p$,[4] where E_{el} is the electric field in the depletion region [~2.5 x 10^5 V/cm], (the entire GaN:Er + GaN film is assumed to be depleted); λ is the mean free path for optical phonon collisions [~5 nm], estimated from the value for Si; and E_p is the energy lost by optical phonon collisions [73 meV].[75] This gives an electron kinetic energy on the order of 0.5 eV. Assuming a distribution of energies around that mean, a fraction of the accelerated electrons would have sufficient energy to excite the Er^{3+} ions (at least 0.8 eV). This is similar to electroluminesce observed in high oxygen-content semi-insulating polycrystalline Si (SIPOS) structures biased at 20 V as demonstrated by Lombardo et al[76] and in GaN:Er on Al_2O_3 devices formed by ion implantation.[77] Higher GaN:Er/Si device biases would likely result in higher Er^{3+} electroluminescent intensity as the average electron kinetic energy approaches the $^4I_{11/2}$ Er^{3+} pump level at approximately 1.2 eV (Figure 1-2) as was observed in the case of implantation-formed GaN:Er LEDs where biases in excess of 100 V were used to produce 1.54 μm electroluminescence intensities comparable to PL intensities. Also, the relatively high-resistivity p-Si substrate (~10 Ω-cm) and the undoped GaN and AlN buffer layers probably contribute significant series resistance to the overall voltage drop through the device. Ideally, the optically active regions of an electroluminescent GaN:Er device would be in contact with conductive injection layers such as in the n-Schottky and p-i(Er)-n structures shown in Figure 6-4 grown on low-resistivity Si.

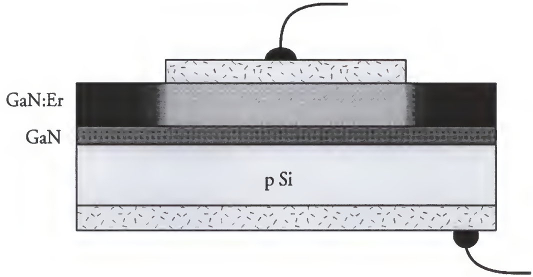

FIGURE 6-1. Cross-section diagram of the metal-GaN:Er-Si electroluminescent device structure.

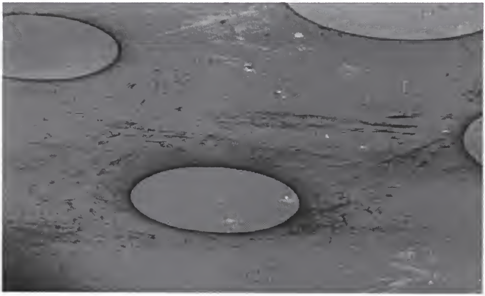

FIGURE 6-2. Scanning electron micrograph (600X) of the metallized surface of an LED-processed GaN:Er sample.

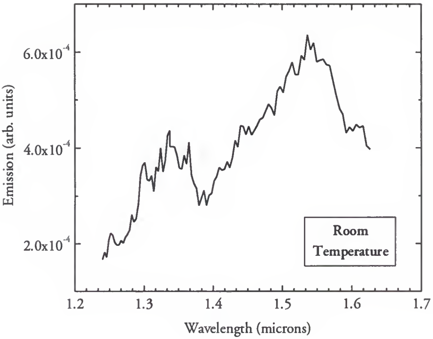

FIGURE 6-3. Room-temperature electroluminescence spectra of the GaN:Er device structure outlined in Figure 6-2. Spectra was taken at 20 V reverse bias.

However, growing such structures with plasma-assisted MOMBE presents a challenge in terms of impurity distributions. As seen in the growth experiments outlined in Chapter 5, the presence of high concentrations of carbon and oxygen from the metalorganic precursor are important for the optical activation of Er^{3+}. However, the presence of these impurities is also known to passivate electrical dopants in GaN. For example, magnesium, the most common p-type dopant currently used in GaN, is known to have a high affinity for oxygen. Attempts to produce p-type triethylgallium-derived GaN:Mg using bis-(cyclopentadienyl) magnesium and n-type GaN:Si using $SiBr_4$ with plasma-assisted MOMBE failed. However, n-type (10^{19} cm^{-3}) and p-type (10^{16} cm^{-3}) GaN has been attained using 8N purity solid Ga metal evaporated from

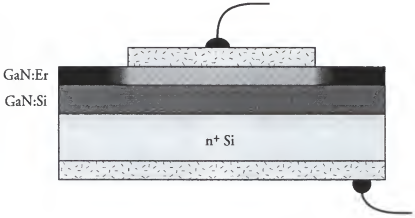

GaN:Er Schottky Structure

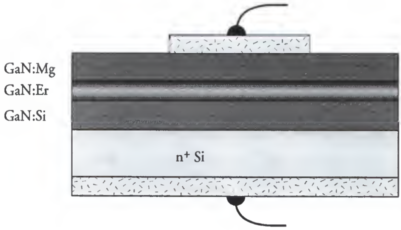

GaN:Er pin Structure

FIGURE 6-4. Cross-section diagrams of GaN:Er/GaN:Si/n$^+$ Si Schottky (top) and GaN:Mg/GaN:Er/GaN:Si/n$^+$ Si p-i-n (bottom) diode structures.

an effusion cell at approximately 950 °C as the Group III source. In order to produce p-i(Er)-n and n-Schottky structures like those depicted in Figure 6-4, that would be both optically and electrically active, triethylgallium was used as the Group III source during the growth of the insulating, Er-containing layers and solid Ga was used during the deposition of n- or p-type injection layers. The magnesium, erbium and silicon profiles, as determined by SIMS are shown in Figure 6-5. The strongly-luminescent TEGa-derived GaN:Er films that produced the strong room-temperature PL depicted in Figure 5-2 had carbon and oxygen backgrounds of 10^{21} cm^{-3} and 10^{20} cm^{-3}, respectively. However, SIMS indicates that the C and O concentration in the TEGa-derived GaN:Er layer of the p-i-n structure are 2×10^{19} cm^{-3} and 2×10^{18} cm^{-3}, respectively. The Er^{3+} PL from this p-i-n structure is also significantly less intense than that observed from the TEGa-derived films grown previously. This variability in impurity background is likely due to the volatility of the ether in the TEGa source causing the ether to distill out over time. This results in a drop in the ether-associated impurity concentrations in TEGa-derived GaN over the lifetime of the TEGa bubbler charge.

To further elucidate the impact of C and O on Er^{3+} activation, ion-implantation was used to introduce C and O into the p(Mg)-i(Er)-n(Si) structure grown on n^+-Si depicted in Figure 6-5. A 2×10^{15} cm^{-3} dose of carbon was implanted into the p-i-n structure at 200 keV to create a carbon profile with a peak concentration of $\sim 10^{20}$ cm^{-3} at a depth that coincided with the Er-doped layer. A second piece of the p(Mg)-i(Er)-n(Si) sample was implanted with a 2×10^{15} cm^{-3} dose of oxygen at 250 keV to create an oxygen profile with a peak concentration of $\sim 10^{20}$ cm^{-3} centered at approximately the same depth as the Er-doped layer. The carbon and oxygen implant parameters were arrived at through iterative implant simulations using an Implant Sciences software package. These simulated implant profiles are shown in Figure 6-6. After implantation, the room-temperature Er^{3+} PL from the p-i-n structure was dramatically attenuated indicating that implantation damage produces a high concentration of states that compete non-radiatively with or channel energy out of the Er ion. Upon annealing at 625°C the Er^{3+} signal returned in both the carbon- and oxygen-implanted samples. As shown in Figure 6-7, after 930 seconds of annealing, the 1.54 μm signal in both the C- and O-implanted samples increased beyond the intensity measured for unimplanted samples, either unannealed or annealed. Carbon

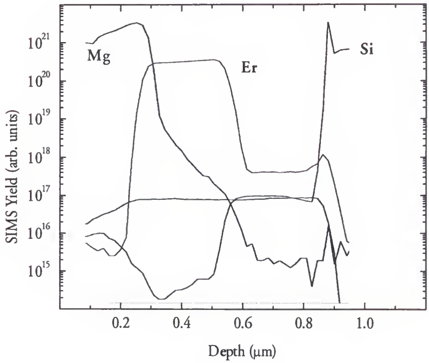

FIGURE 6-5. Secondary ion mass spectrometry profiles of the Mg-, Er-, and Si-doped layers of an MOMBE-derived p-i-n structure.

implantation induced a larger increase in Er^{3+} activation than oxygen implantation. This follows the results seen for Si:Er co-implantation by Michel et al.[11]

Exciton-based energy transfer models have been proposed for excitations in Si:Er[78] and GaP:Er.[10] In the Si:Er model, intra-Er Auger excitation from excitons is mediated by a gateway state in the gap. This mechanism, including other radiative and non-radiative pathways are illustrated in Figure 6-8. This model assumes that some mid-gap level exists at an energy conducive to transferring energy directly to the 4f levels of Er^{3+}. The existence of such a level also suggests the possibility of back-transfer processes where excited Er complexes could transfer an excited carrier back to this mid gap state which is subsequently thermalized up into the conduction band, effectively deactivating the erbium center. This model may be relevant to the GaN:Er luminescence mechanism observed in this study as the importance of carbon and oxygen co-doping have been well established. The fact that carbon has a greater impact on Er^{3+} luminescence efficiency than the more electronegative oxygen implies that ionic field effects are not of primary importance. Rather, it may be the introduction of beneficial mid-gap states that provide efficient energy transfer pathways for Er in GaN.

The effect of energy gap relative to the Er^{3+} pump levels on 1.54 μm PL efficiency was investigated in $In_{1-x}Ga_xAs_yP_{1-y}$ indicating that indirect energy transfer processes dominate rare-earth excitation in this material.[79] A diagram of this excitation model is shown in Figure 6-9. Only after the band energy was increased to 70 meV greater than the Er ($^4I_{11/2}$ - ground state) energy did the photoluminescence efficiency increase substantially. This strongly suggests that carrier/exciton-trapping, associated with a Coulombic field or a deformation potential around the substitutional Er ion, controls energy transfer to Er^{3+}. In rare earth-doped II-IV semiconductors, donor-acceptor pairs (DAPs) are believed to play the dominant role in excitation through

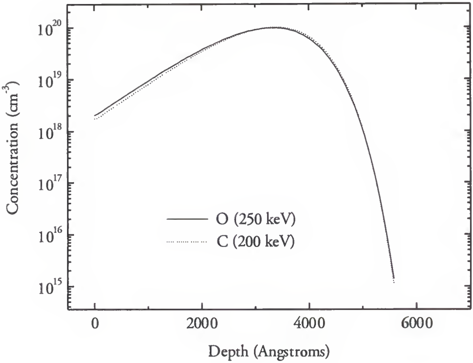

FIGURE 6-6. Computer simulations of a 250 keV oxygen implant and a 200 keV carbon implant into GaN.

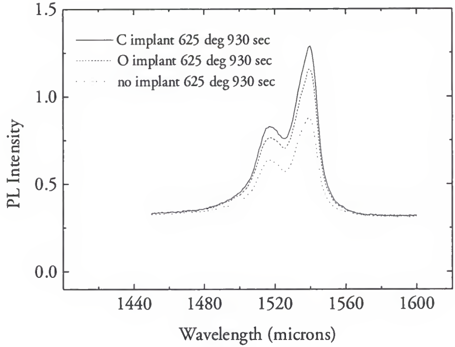

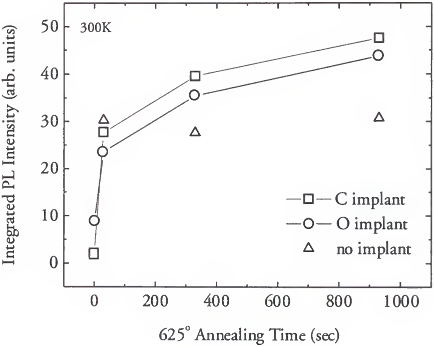

FIGURE 6-7. Effect of 625°C rapid-thermal-annealing on the Er^{3+} PL from O- and C-implanted GaN:Er p(Mg)-i(Er)-n(Si) structures. The top figure compares the spectra of implanted and unimplanted samples after annealing. The bottom plot shows the integrated 1.54 μm PL intensity as a function of annealing time for unimplanted and implanted samples.

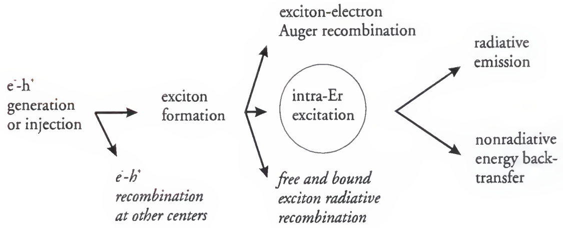

FIGURE 6-8. Energy flow diagram of Er^{3+} excitation proposed for Si:Er.[78]

localization of excitons.[80] Cathodoluminescence and PL results indicated a strong energy coupling from excited DAPs to the 4f levels of closely-associated rare-earth ions.[81] A component of the DAP may act as activator and sensitizer, such as an acceptor that provides a recombination trap pathway and compensates rare-earth ion charge. This may be particularly relevant to MOMBE-derived GaN:Er. In Chapter 4, the strongest 1.54 µm PL was observed for GaN:Er with high [C] and [O] backgrounds. Previously, carbon has been demonstrated to act as a heavily self-compensating acceptor in GaN.[82] Also, in the implantation experiments outlined earlier in this chapter, carbon was seen to have a greater impact on solid source-derived erbium activation than oxygen. Combining the models outlined in Figures 6-8 and 6-9, luminescence enhancement of GaN:Er may result from the introduction of charge-compensating acceptor-like states that provide energy transfer pathways for the excitation and de-excitation of MOMBE-derived GaN:Er. This model is further reinforced by initial experiments conducted with n-type InAlN:Er, which is characterized by high carbon backgrounds associated with the use of TMIn, and the observation of temperature-dependent 1.54 μm photoluminescence lifetimes for high [C] and [O] GaN:Er.

Preliminary studies of Er^{3+} PL intensity as a function of InN mole fraction in $In_xAl_{1-x}N$:Er ternaries indicate that the onset of n-type conductivity may suppress Er^{3+} optical activation. Figure 6-10 shows the integrated Er^{3+} 1.54 μm PL intensity, normalized to the AlN:Er signal, for several $In_xAl_{1-x}N$:Er compositions. Initially, at low Indium content, where the film is still electrically-depleted, an increase in PL intensity was observed. This increase in Er^{3+} intensity may be due to an increase in structural quality as the growth temperature of the In-containing ternaries (525 °C) is closer to the optimal temperature for the deposition of InN as compared to the

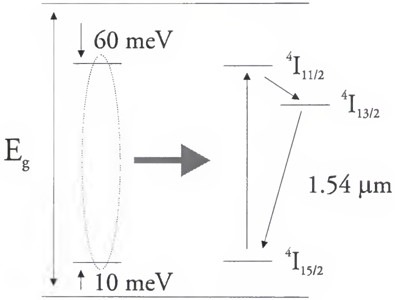

FIGURE 6-9. Energy diagram of exciton-trapping and energy transfer to the 4f levels of the Er^{3+} ion as proposed by Wellman et al.[79]

relatively higher temperatures associated with high-quality AlN growth. This reduction in AlN structural quality is evidenced by the observation of lower Er^{3+} PL intensities for MOMBE-derived AlN:Er grown at 625°C compared to luminescence from films grown under otherwise identical conditions at 700°C. At higher InN mole fractions, after the onset of strong n-type conductivity ($n = 10^{20}$ cm^{-3} for $x_{InN} \sim 0.44$) , the PL drops off, possibly due to self compensation of C acceptor-mediated energy transfer to the Er ions by a InN:C shallow donor state. However, the effects of free-carrier absorption of the pump signal may also affect the observed Er^{3+} optical response, especially at higher InN mole fractions. Schottky and p/n diode structures were fabricated from $In_{0.23}Al_{0.77}N$ (n-type) films. After annealing, electroluminescence was observed from the Schottky structure grown on n^+-Si in reverse bias. However, luminescence was not observed from devices fabricated from $In_{0.23}Al_{0.77}N$ deposited on p-GaAs. This is likley due to the fact that reverse bias breakdown in the $In_{0.23}Al_{0.77}N$/p-GaAs sample occurs first in the lower gap GaAs instead of in the Er-doped nitride.

Beneficial effects of light-element co-doping have also been seen in the electroluminescence efficiency of Er in semiconductor hosts.[83] Since erbium excitations act within the parity-forbidden transitions allowed by weak field splitting in the 4f shell, the electric dipole interaction and therefore the electrical impact excitation cross-section of isolated Er ions is quite small. In isolation, the weakly-allowed intra-4f shell erbium transitions, induced by crystal field splitting are expected to have relatively long luminescence lifetimes such as the millisecond-regime lifetimes observed for Er in a number of hosts.[5] Complexing Er with electronegative codopants has been shown to enhance Er^{3+} electroluminescence intensity and reduce thermal quenching. This suggests that the impact excitation cross-section for rare-earth complexes and clusters is consid-

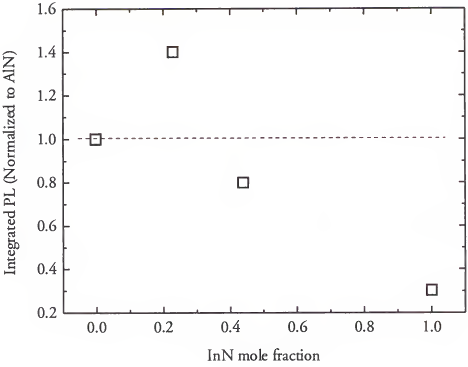

FIGURE 6-10. Integrated Er^{3+} 1.54 μm PL intensity as a function of InN fraction in InAlN doped with Er during MOMBE growth.

erably larger than that of Er alone. This may explain why the high [C] and [O] structure depicted in Figure 6-1 exhibited electroluminescence in spite of the high series resistance, while no electrically-stimulated 1.54 μm signal was detected from the p-i(Er)-n structure. Photoluminescence lifetimes of TEGa-derived GaN were observed to be quite short, on the order of 100 microseconds. Also, the 1.54 μm PL lifetimes decreased with increasing temperature as shown in Figure 6-11. This coincides with the expected luminescence behavior for the mid-gap state-mediated excitation model depicted in Figure 6-8. In this case the probability of phonon-assisted thermalization of electrons out of the mid-gap state, back-transferring energy from the Er^{3+} ion, would increase with temperature following the increase in phonons available to induce such a transition.

As the binding energy of these states increase, larger numbers of thermal phonons would be required to de-trap a carrier. Such a back-transfer process would deactivate excited Er ions, quenching radiative recombination and shortening the luminescence lifetime in agreement with the observed thermal PL quenching and lifetime behavior for MOMBE-derived GaN:Er.

Closer study of the temperature-dependence of the 1.54 µm luminescence lifetime further indicates that co-dopant related transfer states are involved in Er^{3+} excitation in MOMBE-derived GaN:Er. Photoluminescence lifetime and integrated intensity of the 1.54 µm Er^{3+} transition are plotted as a function of temperature for high [C] and [O] GaN:Er in Figure 6-12. Of immediate interest is the functional similarity between the lifetime and integrated intensity, both of which show a maximum near 200 K. As mentioned in the previous paragraph, the 100 microsecond-regime lifetimes are quite short. In Er-doped silica, increases in the fraction of excited Er ions are usually associated with shorter lifetimes.[1] These shorter lifetimes can be attributed to Er-Er interactions, such as cooperative upconversion in which the relaxation of an excited erbium ion directly stimulates another closely associated, excited erbium ion, putting it into a higher energy state which may then relax non-radiatively. This process ultimately leads to the quenching of 1.54 µm radiative emission. An example of this de-excitation process is shown in Figure 6-13. For GaN:Er the opposite behavior was observed. Near 200 K, the increase in 1.54 µm luminescence lifetimes is associated with a corresponding increase in integrated intensity for sub-gap optical pumping. This suggests a thermally-activated state contributes to an increase in the $^4I_{13/2}$ - $^4I_{15/2}$ radiative lifetime. It is proposed that impurity states, associated with carbon, prohibit Er-Er de-excitation interactions and Er back-transfer mechanisms by strongly-trapping excitons and shielding long-range Er ion interactions through localization, and charge compensa-

---

tion. This accounts for the correlation of luminescence lifetime with intensity in TEGa-derived GaN:Er, the growth and implantation results seen previously in this work, and the models for trap- or mid-gap state-mediated Er energy back-transfer processes proposed for other semiconductor:Er systems.

Low temperature cathodoluminescence (CL) spectroscopy of MOMBE-derived GaN:Er was performed by L. J. Brillson and his group at the Ohio State University.[84] Depth-dependent probing of the GaN:Er film with CL showed strong 0.8 eV emission (1554 nm) that corresponded to the Er doping profile. However, the profile of emission lines at 1.8 eV, 2.2 eV, and 2.3 eV, corresponding to other intra-4f shell Er^{3+} transitions[85] showed a noticeable interaction with near-surface defects that evolved with annealing;. Broadband sub-gap emission features, such as 'yellow' luminescence near 2.2 eV were not detected. Also, increases in 1.54 μm Er^{3+} luminescence coincided with a decrease in the band-edge emission intensity. This suggests, in agreement with the photoluminescence lifetimes and impurity enhancement model proposed in this work, that the GaN:Er radiative process is fast and efficient, competing with band edge emission.

In summary of this chapter, electroluminescence from GaN doped with erbium during growth by plasma-assisted MOMBE has been demonstrated. Explicit studies have verified the beneficial impact of light impurities, especially carbon, on GaN:Er luminescence. These results, and the photoluminescence and cathodoluminescence behavior of MOMBE-derived GaN:Er suggest that a thermally activated, acceptor-like state associated with carbon inhibits Er de-excitation.

In conclusion of this dissertation, the growth of III-N:Er semiconductor materials has been developed resulting in the demonstration of 1.54 μm electroluminescence from a

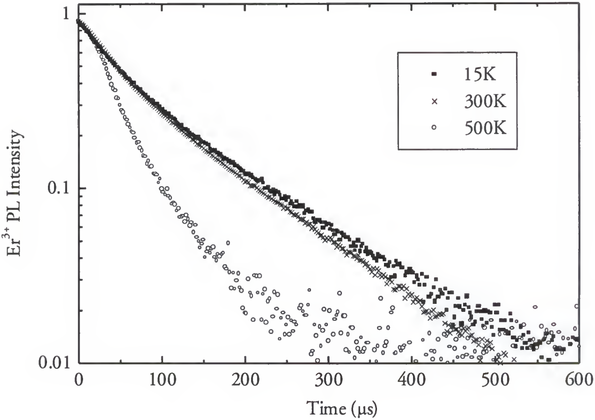

FIGURE 6-11. Photoluminescence decay curves (1.54 μm transition) for TEGa-derived GaN:Er at 15K, 300 K and 500 K.

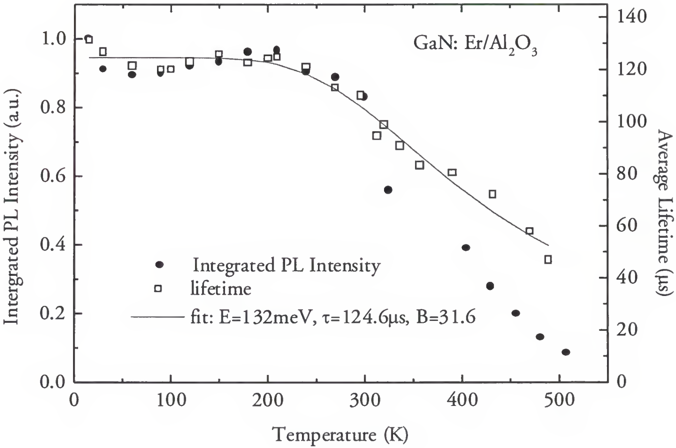

FIGURE 6-12. Photoluminescence lifetime (1.54 μm transition) and intensity as a function of temperature for TEGa-derived GaN:Er.

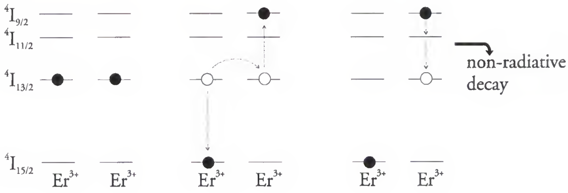

FIGURE 6-13. Energy diagram representing the succesive configurations of closely associated Er^{3+} ions during upconversion de-excitation.

GaN:Er-based device grown directly on Si. For the first time, GaN and AlN have been doped with Er during growth to produce III-N:Er films with strong optical activity at room temperature. Also, for the first time the integration of GaN:Er and InAlN:Er with silicon in devices operating at room temperature has demonstrated the feasibility for III-N:Er near-IR optoelectronics. Impurity issues have been investigated through growth, implantation and luminescence experiments, indicating that carbon can play a dominant role in defect-mediated activation of Er^{3+}. Throughout this research plasma-assisted MOMBE has been shown to be a versatile research tool for exploring new applications of III-N semiconductors.

REFERENCES

1. E. Snoeks, *Optical Doping of Silica by Erbium Ion Implantation*, PhD. Dissertation, Univ of Utrecht,, Netherlands (1995).

2. S. Hufner, *Optical Spectra of Transparent Rare-Earth Compounds*, Academic Press, New York (1978).

3. E. A. Fitzgerald and L. C. Kimmerling, *Mat. Res. Soc. Bull.*, 23 No. 4 (1998) 39.

4. G. N. van den Hoven, PhD. Dissertation, Univ. of Utrecht, Netherlands (1996).

5. J. M. Zavada and D. Zhang, *Sol. State Elec.*, 38 (1995) 1285.

6. V. Swaminathan, A.T. Macrander, *Materials Aspects of GaAs and InP Based Structures*, Prentice Hall, New Jersey (1991).

7. S. M. Sze, *Physics of Semiconductor Devices*, Wiley, New York (1981).

8. E. Desurvire, *Erbium-Doped Fiber Amplifiers: Principles and Applications*, Wiley, New York (1994).

9. P. N. Favennec, H. L'Haridon, M. Salvi, D. Moutonnet and Y. L. Guillou, *Electron. Lett.*, 25 (1989) 718.

10. X. Z. Wang and B. W. Wessels, *Appl. Phys. Lett.*, 64 (1994) 1537.

11. J. Michel, J. L. Benton, R. F. Ferrante, D. C. Jacobson, D. J. Eaglesham, E. A. Fitzgerald, Y. -H. Xie, J. M. Poate, and L. C. Kimmerling, *J. Appl. Phys.*, 70 (1991) 2672.

12. H. Morkoc, S. Strite, G. B. Gao, M. E. Lin, B. Sverdlov, and M. Burns, *J. Appl. Phys.*, 76 (1994) 1363.

13. J. Dean, editor, *Lange's Handbook of Chemistry*, 13th Ed., McGraw-Hill, New York (1985).

14. S. D. Lester , F. A. Ponce , M. G. Craford, D. A. Steigerwald , *Appl. Phys. Lett.* 66 (1995) 1249 .

15. T. Ogino and M. Aoki, *Jap. J. Appl. Phys.*, **19** (1980) 2395.

16. B. -C. Chung and M. Gershenzon, *J. Appl. Phys.*, 72 (1992) 651.

17. J. Han, L. He, R. L. Gunshor and A. V. Nurmikko, *IEEE Circ. and Dev.*, (1994) 18.

18. R. Davis, *Phys. B*, 185 (1993) 1.

19. H. Amano, N. Sawaki, I. Akasaki and Y. Toyoda, *Appl. Phys. Lett.*, 48 (1986) 353.

20. S. Yoshida, S. Misawa and S. Gonda, *J. Vac Sci. Technol. B*, **1** (1983) 250.

21. H. Amano, M. Kito, K. Hiramatsu, and I. Akasaki, *Jap. J. Appl. Phys.*, 28 (1989) L2112.

22. S. Nakamura, M. Senoh, and T. Mukai, *Jap. J. Appl. Phys.* 32 (1993) L8.

23. S. Nakamura, M Senoh, S Nagahama, N Iwasa, T Yamada, T Matsushita, H Kiyoku, Y Sugimoto, *Jap. J. Appl. Phys.*, 35 (1996) L74.

24. S. Nakamura, M. Senoh, S. Nagahama, N. Iwasa, T. Yamada, T. Matsushita, H. Kiyoku, Y. Sugimoto, *Jap. J. Appl. Phys.*, 35 (1996) L217.

25. S. Nakamura, M. Senoh, S. Nagahama, N. Iwasa, T. Yamada, T. Matsushita, H. Kiyoku, Y., *Appl. Phys. Lett.*, 68 (1996) 2105.

26. S. Strite and H. Morkoc, *J. Vac. Sci. Technol. B*, **10** (1992) 1237.

27. S. Nakamura, M. Senoh, S. Nagahama, N. Iwasa, T. Yamada, T. Matsushita, H. Kiyoku, Y. Sugimoto, T. Kozaki, H. Umemoto, M. Sano and K. Chocho, *Jap. J. Appl.Phys.*, 37 (1998) L309.

28. J. L. Vossen and W. Kern, editors, *Thin Film Processes II*, Academic Press, Boston (1991).

29. M. J. Antonell, PhD. Dissertation, Univ. of Fl., (1997).

30. P. van der Wagt, *http://snowmass.stanford.edu/*, Harris Group Web Page, Stanford Univ. (1996).

31. J. D. MacKenzie, S. M. Donovan, C. R. Abernathy, S. J. Pearton, P. H. Holloway, R. Linares, J. Zavada, and B. Chai, *J. Electrochem. Soc.*, **145** (1998) 2581.

32. J. D. MacKenzie, C. R. Abernathy, S. J. Pearton, V. Krishnamoorthy, S. Bharatan, and K. S. Jones, *Appl. Phys. Lett.*, **67** (1995) 253.

33. J. D. MacKenzie, C. R. Abernathy, J. D. Stewart and G. T. Muhr, *J. Cryst. Growth*, 164 (1996) 143.

34. C. R. Abernathy, *Mat. Sci. Eng. Rep.*, R14 No. 5 (1995).

35. R. J. Molnar and T. D. Moustkas, *J. Appl. Phys.* 76, 4587 (1994).

36. T. L. Tansley and Egan, *Phys. B* 185 (1993) 190.

37. T. C. Fu, N. Newman, E. Jones, J. S. Chan, X. Liu, M. D. Rubin, N. W. Cheung, and E. R. Weber, *J. Eect. Mat.*, 24, 249 (1995).

38. R. C. Powell, N. E. Lee, and J. E. Greene, *Appl. Phys. Lett.* 60, 2505 (1992).

39. M. E. Lin, B. Sverdlov, G. L. Zhou, and H. Morkoc, *Appl. Phys. Lett.*, 62, 3479 (1993).

40. A. L. Holmes, K. G. Fertitta, F. J. Ciuba and R. D. Dupuis, *Elect. Lett.*, 30 (1994).

41. W. E. Plano, J. S. Major, Jr., D. F. Welch and J. Speirs, *Elect. Lett.*, 30, 2079 (1994).

42. P. J. Born and D. S. Robertson, *J. Mater. Sci.*, 15 (1980) 3003.

43. K. Matsubara and T. Takagi, *Jap. J. Appl. Phys.*, 22 (1982) 511.

44. Z. Sitar, M. J. Paisly, B. Yan and R. F. Davis, *Mat. Res Soc. Symp. Proc.*, 162 (1990) 537.

45. T. Detchprohm, H. Amano, K. Hiramatsu and I. Akasaki, *J. Cryst. Growth*, 128 (1993) 384.

46. R. G. Wilson, B. L. H. Chai, S. J. Pearton, C. R. Abernathy, F. Ren, and J. M. Zavada *Appl. Phys. Lett.*, 69 (1996) 3848.

47. P. Maki and B. Chai, presented at the Materials Research Society, Boston, MA (1995).

48. C. R. Abernathy, J. D. MacKenzie, S. R. Bharatan, K. S. Jones and S. J. Pearton, *Appl. Phys. Lett.*, 66 (1995) 1632.

49. S. DenBaars, Abstract 296, *Electrochem. Soc. Meet. Abstr.*, 96-1, Los Angeles, CA, May 5-10, 1996.

50. J. D. MacKenzie, C. R. Abernathy, S. J. Pearton, U. Hömmerich, M. Thaik, X. Wu, F. Ren, R. G. Wilson and J. M. Zavada, *Mat. Res. Soc. Proc.* 468 (1997).

51. N. Newman, *Electrochem. Soc. Proc.*, 96-11 (1996) 1.

52. I. Akasaki and H. Amano, *J. Electrochem. Soc.*, 141-8 (1994) 2266.

53. R. J. Molnar and T. D. Moustakas, *J. Appl. Phys.*, 76 (1994) 15.

54. W. C. Hughes, W. H. Rowland, Jr., M. A. L. Johnson, S. Fujita, J. W. Cook, and J. F. Schetzina, *J. Vac. Sci. Tecnol.*, **B** 13 (1995) 1571.

55. R. C. Powell, G. A. Tomasch, Y. W. Kim, J. A. Thornton, and J. E. Greene, *Mater. Res. Soc. Symp. Proc.*, 162 (1990) 525.

56. M. Rubin, N. Newman, J. S. Chan, T. C. Fu and J. T. Ross, *Appl. Phys. Lett.*, **64** (1994) 64.

57. M. V. Averyanova, S. Yu. Karpov, Yu. N. Makarov, I. N. Przhevalskii, M. S. Ramm, R. A. Talolaev, *MRS Internet J. Nitride Semicond. Res.*, 1 (1996) 31.

58. S. Coffa, F. Priolo, G. Franzo, V. Bellani, A. Carnera, C. Spinella, *Phys. Rev. B*,48 (1993) 11 782.

59. R. G. Wilson, R. N. Schwartz, C. R. Abernathy, S. J. Pearton, N. Newman, M. Rubin, T. Fu, and J. M. Zavada, *Appl. Phys. Lett.*, 65 (1994) 992.

60. A. J. Neuhalfen and B. W. Wessels, Appl. Phys. Lett., 59 (1991) 2317.

61. A. N. Nesmeianov, *Vapor Pressure of the Chemical Elements.*, Elsevier, New York (1963).

62. H. Ennen, J. Schneider, G. Pomrenke, and A. Axman, *Appl. Phys. Lett.*, 43, 943 (1983).

63. P. B. Klein and G. S. Pomrenke, *Electron. Lett.* 24, 1503 (1988).

64. D. J. Eaglesham, J. Michel, E. A. Fitzgerald, D. C. Jacobson, J. M. Poate, J. L. Benton, A. Polman, Y. -H. Xie, and L. C. Kimmerling, *Appl. Phys. Lett.*, 58, 2797 (1991).

65. A. Polman, J. S. Custer, E. Snoeks, and G. N. van den Hoven, *Nucl. Instr. Meth.* **B80/81**, 653 (1993).

66. A. Kozanecki, M. Chan, C. Jeynes, B. Sealy, and K. Homewood, *Solid State Commun.*, 78 (1991) 763.

67. Y. S. Tang, J. Zhang, K. C. Heasman, and B. J. Sealy, *Solid State Commun.*, 72 991 (1989).

68. J. Nakata, M. Taniguchi, and K. Takahei, *Appl. Phys. Lett.*, **61** (1992) 2665.

69. B. W. Wessels, *Mat. Res. Soc. Symp. Proc.*, 422 (1996) 247.

70. C. H. Qiu, M. W. Leksono, J. I. Pankove, J. T. Torvik, R. J. Feuerstein and F. Namavar, *Appl. Phys. Lett.*, 69 (1996) 2098.

70. J. M. Zavada, R. G. Wilson, R. N. Schwartz, J. D. MacKenzie, C. R. Abernathy, S. J. Pearton, X. Wu, and U. Hommerich, *Mat. Res. Soc. Symp. Proc.*, 422 (1996) 193.

72. E. Silkowski, Y. K. Yeo, R. L. Hengehold, B. Goldenberg and G. S. Pomrenke, *Mat. Res Soc. Proc.*, 422 (1996) 69.

73. S. Kim, S. J. Rhee, D. A. Turnbull, X. Li, J. J. Coleman and S. G. Bishop, *Mat. Res. Soc. Proc.*, 468 (1997) 131.

74. U. Hommerich, M. Thaik, R. N. Schwartz, R. G. Wilson, J. M. Zavada, S. J. Pearton, C. R. Abernathy and J. D. MacKenzie, *Electrochem. Soc. Proc.*, 98-2 (1998) 110.

75. A. Cros., H. Angerer, R. Handschuh, O. Ambacher and M. Stutzmann, *Mat. Res. Soc. J. Nitr. Sem. Res.*, 2 (1997) 43.

76. S. Lombardo, S. U. Campisano, G. N. van den Hoven and A. Polman, *Appl. Phys. Lett.*, 77 (1995) 6504.

77. J. Torvik, R. J. Feuerstein, J. I. Pankove, C. H. Qiu, and F. Namavar, *Appl. Phys. Lett.* 69 (1996) 2098.

78. J. Michel, B. Zheng, J. Palm, E. Oullette, F. Gan, and L. C. Kimmerling, *Mat. Res. Soc. Proc.*, 422 (1996) 317.

79. P. Wellman, A Winnacker, and G Pensl, *Mat. Res. Soc. Proc.*, 422, (1996) 255.

80. M. Godlewski, *Mat. Res. Soc. Symp. Proc.*, 422 (1996) 291.

81. D. Hommel, W. Busse, H.-E. Gumlich, D. Suisky, J. Rosler, K. Swiatek, and M. Godlewski, J. Cryst. Growth, **101** (1990) 393.

82. C. R. Abernathy, J. D. MacKenzie, S. J. Pearton, W. S. Hobson, *Appl. Phys. Lett.*, 66 (1995) 1969.

83. G. Franzo, F. Priolo, S. Coffa, A. Polman, and A Carnera, *Nucl. Instr. and Meth. in Phys. Res. B*, 96 (1995) 374.

84. T. Levin, I. Shafer, A. P. Young, L. J. Brillson, J. D. MacKenzie, and C. R. Abernathy, *Amer. Vac. Soc. 45th Int. Symp.*, Abstract (1998) 1337.

85. M. Thaik, U. Hommerich, R. N. Schwartz, R. G. Wilson and J. M. Zavada, *Appl. Phys. Lett.*, 71 (1997) 2641.

BIOGRAPHICAL SKETCH

Born on Long Island, New York on a snowy 27th of January, 1971, I was soon transplanted to the Southeast. I spent my childhood wandering around the suburban woods of Gastonia, North Carolina, Macon, Georgia, and Rockledge, Florida. Maybe it was the fact that I was constantly a stranger that spurred my interests in academics. At any rate, by the time I was a fourth grader I had decided I wanted to be a physicist. A few years later, after talking my parents out of sending me to Catholic high school on the basis that the public high school had a better science program, I found myself spending the majority of my high school years working on various science projects on topics ranging from photovoltaics to superconductors, under the direction of Phillip Rose.

Upon graduating from high school I enrolled as an undergraduate at the Massachusetts Institute ofTechnology in Cambridge, Massachusetts. After a year studying and working in the strange heirarchy of the Physics Department, I realized that my research and career interests would be better pursued studying electronic materials in the Materials Science and Engineering Department. There I came toknow, work for, and argue, with Professor Kirk Kolenbrander who remains, to this day, a very important part of my academic trials and successes. Through the teaching of Prof. Kolenbrander and others, I became very interested in semiconductors and optoelectronics and was able to develop those interests during the summers working for AT&T Bell Laboratories in Murray Hill, New Jersey and AT&T Microelectronics in Orlando, Florida.

Under Prof. Kolenbrander's guidance I finished my senior research thesis on in-situ laser spectroscopy of Si nanoparticles for which I recieved the undergraduate thesis award from the materials department. After being wrenched through some demoralizing personal traumas which had nothing to do with academics and quite a bit to do with being in the wrong place at the wrong time, I ended up, once again, heading South.

In the Spring of 1994 I met Prof. Cammy Abernathy at the University of Florida. She had just arrived in the materials department herself from AT&T Bell Laboratories with a few truckloads of crystal growth equipment and a desire to hit the academic ground running. I quickly realized that I could not hope to find a more capable or more reasonable person with whom to do graduate research and I became Cammy's first graduate student. After a few years of moving heavy objects, plumbing, wiring, and growing films I became ready to face the realities of having to become a professional scientist, leaving school, and finding something interesting to do for few the remaining years I have left before senility sets in. With the love and support of my finace Lynn, of whom I will someday be worthy of, my mom and dad, and my dog Maxwell I have decided to do the only sensible thing for me, return to school. Upon receiving my PhD. I plan to accept a post-doctoral research associate position in the Cavendish Laboratory at Cambridge University working under Prof. Richard Friend on materials issues in conjugated polymer physics. I plan to spend my postdoctoral tenure doing what I have always done, trying to learn, and resisting the pull of the unexplainable beauty and fascination of diving in the clear water of North Florida's springs and caves.

I certify that I have read this study and that in my opinion it conforms to acceptable standards of scholarly presentation and is fully adequate, in scope and quality, as a dissertation for the degree of Doctor of Philosophy.

Cammy R. Abernathy, Chair
Professor of Materials Science
and Engineering

I certify that I have read this study and that in my opinion it conforms to acceptable standards of scholarly presentation and is fully adequate, in scope and quality, as a dissertation for the degree of Doctor of Philosophy.

Paul H Holloway

Paul Holloway
Professor of Materials Science
and Engineering

I certify that I have read this study and that in my opinion it conforms to acceptable standards of scholarly presentation and is fully adequate, in scope and quality, as a dissertation for the degree of Doctor of Philosophy.

Rajiv Singh
Professor of Materials Science
and Engineering

I certify that I have read this study and that in my opinion it conforms to acceptable standards of scholarly presentation and is fully adequate, in scope and quality, as a dissertation for the degree of Doctor of Philosophy.

Stanley Bates

Stanley Bates
Associate Engineer of Materials Science
and Engineering

I certify that I have read this study and that in my opinion it conforms to acceptable standards of scholarly presentation and is fully adequate, in scope and quality, as a dissertation for the degree of Doctor of Philosophy.

Fred Sharifi

Fred Sharifi
Assistant Professor of Physics

This dissertation was submitted to the Graduate Faculty of the College of Engineering and to the Graduate School and was accepted as partial fulfillment of the requirements for the degree of Doctor of Philosophy.

August 1998

Winfred M. Phillips
Dean, College of Engineering

Karen A. Holbrook
Dean, Graduate School